

Spectroscopic Properties of QSOs Selected from Ultraluminous Infrared Galaxy Samples

X.Z. Zheng

*National Astronomical Observatories, Chinese Academy of Sciences,
Datun Road A20, Chaoyang District, Beijing 100012, China*

zxz@alpha.bao.ac.cn

X.Y. Xia

*Department of Physics, Tianjin Normal University,
Weijin Road, Tianjin 300074, China*

xyxia@bac.pku.edu.cn

S. Mao

Univ. of Manchester, Jodrell Bank Observatory, Macclesfield, Cheshire SK11 9DL, UK

smao@jb.man.ac.uk

H. Wu

*National Astronomical Observatories, Chinese Academy of Sciences,
Datun Road A20, Chaoyang District, Beijing 100012, China*

wu@bac.pku.edu.cn

and

Z.G. Deng

Department of Physics, Graduate School, Chinese Academy of Sciences, Beijing 100080, China

dzg@bac.pku.edu.cn

ABSTRACT

We performed spectroscopic observations for a large infrared QSO sample with a total of 25 objects. The sample was compiled from the QDOT redshift survey, the 1 Jy ULIRGs survey and a sample obtained by a cross-correlation study of the IRAS Point Source Catalogue with the ROSAT All Sky Survey Catalogue. Statistical analyses of the optical spectra show that the vast majority of infrared QSOs have narrow permitted emission lines (with FWHM of $H\beta$ less than 4000 km s^{-1}) and more than 60% of them

are luminous narrow line Seyfert 1 galaxies. Two of the infrared QSOs are also classified as low ionization BAL QSOs. More than 70% of infrared QSOs are moderately or extremely strong Fe II emitters. This is the highest percentage of strong Fe II emitters in all subclasses of QSO/Seyfert 1 samples. We found that the Fe II to $H\beta$ line ratio is significantly correlated with the [O III] $\lambda 5007$ peak and $H\beta$ blueshift. Soft X-ray weak infrared QSOs tend to have large blueshifts in permitted emission lines and significant Fe II 48, 49 (5100–5400 Å) residuals relative to the Boroson & Green Fe II template. If the blueshifts in permitted lines are caused by outflows, then they appear to be common in infrared QSOs. As the infrared-selected QSO sample includes both luminous narrow line Seyfert 1 galaxies and low ionization BAL QSOs, it could be a useful laboratory to investigate the evolutionary connection among these objects.

Subject headings: galaxies: Seyfert — quasars: emission lines — quasars: general

1. Introduction

Two of the most important reasons for investigating the ultraluminous IRAS galaxies (ULIRGs) are to find the evolutionary connection between circumnuclear massive starbursts and active galactic nuclei (AGNs) and to identify the evolution path from galaxy mergers to elliptical galaxies and QSOs (see Sanders & Mirabel 1996 for a review). In recent years, significant progress has been achieved with both space and ground-based telescopes (Surace et al. 1998; Surace, Sanders, & Evans 2000; Genzel et al. 1998; Farrah et al. 2001 and reference therein). It is now widely accepted that the vast majority ($\gtrsim 95\%$) ULIRGs are strongly interacting and merging galaxies while some of them are post-merger galaxies. The AGN phenomenon probably appears at the final merging stage (e.g., Clements et al. 1996; Kim, Veilleux, & Sanders 1998; Zheng et al. 1999; Canalizo & Stockton 2001a; Cui et al. 2001). Spectral analyses for large samples of ULIRGs reveal that the fraction of objects with AGN spectral characteristics is about 25–30% while the fraction of QSOs/Seyfert 1s is less than 10% (Wu et al. 1998; Lawrence et al. 1999). However, the percentage of QSOs/Seyfert 1s increases with increasing infrared luminosity, reaching 30–50% for $L_{\text{IR}} > 10^{12.3} L_{\odot}$ (Veilleux, Kim, & Sanders 1999). As the infrared luminosity of ULIRGs is equivalent to the bolometric luminosity of optically selected QSOs (Sanders 2001), we find it convenient to refer to QSOs/Seyfert 1s selected from ULIRGs as IR QSOs throughout this paper.

Previous spectroscopic studies of small and statistically incomplete IR QSO samples have uncovered some unusual properties compared with optically selected QSOs/Seyfert 1s. Many IR QSOs are extremely strong Fe II emitters ($\text{Fe II } \lambda 4570/H\beta > 2.0$), for example, PHL 1092, IRAS 07598+6508 and Mrk 231 (Lípari 1994; Lawrence et al. 1997). In fact, almost 100% of extremely strong Fe II emitters are luminous IR QSOs (Lípari et al. 2002). More than twenty years after their discovery, the origin of such extremely strong optical Fe II emissions in QSOs/Seyfert 1s is still being debated. It has become clear, however, that the strength of the Fe II emission cannot

be explained in the framework of photoionization excitation. If strong outflows and shocks are present in strong/extremely strong Fe II emitters, non-radiative shock heating and overabundance of iron may help to explain the strong Fe II emission (Collin & Joly 2000). Studies of IR QSOs may therefore shed new light on the origin of the Fe II emission.

Furthermore, the fraction of low ionization broad absorption line QSOs (lo-BAL QSOs) is much higher in an IR QSO sample (27%) than that in an optically selected QSO sample (1.4%) (Boroson & Meyers 1992). The lo-BAL QSOs are defined as a subclass of broad absorption line QSOs with an obvious Mg II $\lambda\lambda 2795, 2802$ doublet and low-ionization line absorption troughs (Weymann et al. 1991). Some IR QSOs belong to yet another class of unusual AGNs, the luminous narrow line Seyfert 1s (hereafter NLS1s, Osterbrock & Pogge 1985). NLS1s are defined by their optical emission line properties. They have narrow hydrogen Balmer lines with typical full width at half maximum (FWHM) $\approx 500\text{--}2000 \text{ km s}^{-1}$. The [O III] $\lambda 5007/\text{H}\beta$ line ratio is less than 3 and most of them have strong Fe II emissions. In the X-ray band, NLS1s show systematically steeper power-law slopes in the continuum than normal Seyfert 1s. Some NLS1s exhibit rapid X-ray variabilities as well (Boller, Brandt & Fink 1996). Moran, Halpern, & Helfand (1996) pointed out that many NLS1s are luminous in the infrared band. IR QSOs therefore offer a unique opportunity to investigate potential physical connections between IR QSOs, lo-BAL QSOs and luminous NLS1s (Brandt & Gallagher 2000; Canalizo & Stockton 2001b; Sanders & Mirabel 1996).

In this paper, we study the spectroscopic properties of IR QSOs based on a large sample of 25 objects. We compare their properties with those of the Boroson & Green (1992, hereafter BG92) sample, which includes 87 optically selected QSOs. The outline of the paper is as follows. In §2, we discuss how our IR QSO sample is compiled. The observations and data reduction are described in §3. We present the spectra and statistical properties of our sample IR QSOs in §4 and finally, in §5, we discuss and summarize our results. Throughout this paper we use a Hubble constant of $H_0 = 50 \text{ km s}^{-1} \text{ Mpc}^{-1}$ and $\Omega_0 = 1$ and no cosmological constant. As all our objects have redshift lower than 0.35, the adoption of a different density parameter and cosmological constant has little effects on our results.

2. Sample Selection

Our IR QSO sample is compiled mainly from three sources

- The QDOT redshift survey is a survey of the IRAS galaxies sparse-sampled at a rate of one in six. It includes 2387 IRAS galaxies complete down to a $60 \mu\text{m}$ flux density limit of 0.6 Jy. Lawrence et al. (1999) gave a table of 97 ULIRGs (for $H_0 = 50 \text{ km s}^{-1} \text{ Mpc}^{-1}$ and $\Omega_0 = 1$) with the criterion that the $60 \mu\text{m}$ luminosity is greater than $10^{12} L_\odot$. The optical spectral features and classifications are given in the ULIRG table. There are eight objects in the table identified as IR QSOs.

- Kim & Sanders (1998) selected 118 ULIRGs (infrared luminosities $L(8\text{--}1000\ \mu\text{m}) > 10^{12} L_{\odot}$ for $H_0 = 75\ \text{km s}^{-1} \text{Mpc}^{-1}$ and $\Omega_0 = 0$) from the criterion of $60\ \mu\text{m}$ flux density greater than $1\ \text{Jy}$ in sky region of $\delta > -40^\circ$ and $|b| > 30^\circ$. Veilleux et al. (1999) gave the spectroscopic features and classification of 108 out of these 118 ULIRGs. There are 10 IR QSOs among these 108 ULIRGs.
- Moran et al. (1996) presented spectroscopic classifications for a catalogue of IRAS galaxies selected from the cross-correlation of the IRAS Point Source Catalogue with the ROSAT All Sky Survey by Boller et al. (1992). This catalogue consists of 241 objects and 80 of them are identified as QSOs/Seyfert 1s. 11 of these objects are IR QSOs.

Due to the constraint of the observatory site and instrumental capability, we selected our targets by requiring the IR QSOs to be in the northern sky ($\delta > -30^\circ$) and $z < 0.35$ with $L(8\text{--}1000\ \mu\text{m}) > 10^{12} L_{\odot}$ for $H_0 = 50\ \text{km s}^{-1} \text{Mpc}^{-1}$ and $\Omega_0 = 1$. In addition, we included F09427+1929 (Zheng et al. 1999). Taking into account the overlapping sources, the sample consists of 25 IR QSOs. Table 1 lists the basic parameters. Note that all the infrared luminosities have been converted using $H_0 = 50\ \text{km s}^{-1} \text{Mpc}^{-1}$ and $\Omega_0 = 1$.

While the sample size is still moderate, it is interesting to put this number in the context of the total expected number of IR QSOs in the local universe. The PSCz catalogue provides a complete redshift survey of 15411 IRAS galaxies (Saunders et al. 2000). About 900 ULIRGs were found, which implies the percentage of ULIRGs in the IRAS galaxy catalogue is about 6%. The percentage of IR QSOs among ULIRGs is approximately 10%, as there are 8 IR QSOs among 97 ULIRGs in the QDOT catalogue and 10 IR QSOs among 108 ULIRGs in the 1 Jy sample. So the fraction of IR QSOs in the complete PSCz catalogue is of the order of 0.6%, i.e., the total IR QSOs in the PSCz catalog may be less than 100. Our sample therefore includes roughly one quarter of IR QSOs in the local universe. Statistical results based on this quite large IR QSO sample should be representative.

3. Observations and Data Reduction

Long-slit optical spectroscopic observations were carried out on the 2.16m telescope at the Xinglong station of the National Astronomical Observatories. The observations were mostly performed between October 1998 and November 1999 using an OMR spectrograph while some preliminary studies were conducted before 1998. For our 1998 and 1999 observations, a Tektronix 1024×1024 CCD was used giving a wavelength coverage of $4000\ \text{\AA}$ to $9000\ \text{\AA}$ with a grating of $200\ \text{\AA mm}^{-1}$. The spectral resolution was $9.7\ \text{\AA}$ (2 pixels). The slit width varied from $1.5''$ to $3.5''$ to match the seeing at the Xinglong station. For the pre-1998 observations, the instrument setup was slightly different. For these observations, a grating of $195\ \text{\AA mm}^{-1}$ was used and the coverage is from $3500\ \text{\AA}$ to $8100\ \text{\AA}$ with a resolution of $9.3\ \text{\AA}$. For F01572+0009, the spectrum coverage was in the range of $3800 \sim 6300\ \text{\AA}$ with a resolution of $4.9\ \text{\AA}$. The observation log is given in Table 2 listing

observation epochs, exposure times, approximate seeings and adopted slit widths.

Data reduction was performed using IRAF software. CCD reductions included bias subtraction, flat field correction and cosmic-ray removal. Sky light subtractions were accomplished during the extraction procedure. Wavelength calibrations were carried out using a He-Ar lamp. The resulting wavelength accuracy is better than 1 Å. KPNO standard stars were observed for flux calibrations. The telluric O₂ absorption bands near 6870 Å and 7620 Å were removed using the spectra of the standard stars.

The IRAF package ‘SPLOT’ is used to measure isolated emission lines. ‘SPECFIT’¹, an interactive spectral analysis procedure linked to IRAF is used to measure blended lines (e.g., H α and [N II] $\lambda\lambda$ 6548,6583). It can match a wide variety of emission lines, absorption lines, and continuum models. We model the emission lines with Gaussian profiles and the local continuum as a power-law.

Since the intrinsic extinction of ULIRGs is significant, the Galactic extinction is ignored in our analysis. The extinction correction is calculated approximately according to Veilleux & Osterbrock (1987) and the intrinsic broad line H α /H β ratio is taken to be 3.1 (Baker 1997). The H β /H γ ratio is used to estimate the extinction when H α is out of the spectral coverage (Osterbrock 1989). The measured fluxes of Balmer lines are the sum of the narrow and broad components. It is noted that the intrinsic broad Balmer line ratios may be larger than the adopted values (e.g. MacAlpine 1985) and the extinction corrections may have large uncertainties. Fortunately, the emission line ratios adopted in our analyses, e.g. Fe II λ 4570/H β and [O III] λ 5007/H β , are almost independent of extinction, due to the adjacency of the involved lines. For the Fe II residual measurement, the uncertainty from the extinction correction will be discussed in section 4.3. In general, the uncertainty for the flux measurement introduced by the extinction correction is less than 20%.

As the Fe II emission is moderately or extremely strong for most of our sample galaxies, Fe II multiplets seriously blend with the H β and [O III] $\lambda\lambda$ 4959,5007 lines and contaminate the continuum. We carefully remove the Fe II multiplets following BG92. Their method uses an Fe II template derived empirically from high quality data of I ZW 1, a typical NLS1 galaxy. We then measure the flux for all emission lines based on the Fe II-subtracted continuum. On the other hand, the emission lines for a quite large fraction of our sample IR QSOs show a remarkable asymmetric profile. In such cases, double-Gaussian profiles are needed to fit them. The asymmetry and blueshift can then be measured from the fitting. In the following subsections we describe in more detail the Fe II multiplets removal method and the measurement of the line asymmetry and blueshift.

¹SPECFIT is developed and kindly provided by Gerard A. Kriss.

3.1. Fe II Multiplets Removal

In order to estimate the Fe II strength and measure the line fluxes reliably, we adopt the BG92 method which relies on an Fe II template. The template and observed spectra are both transformed into the rest frame. The template is broadened by convolving with a Gaussian of various line widths and scaled by multiplying by a factor indicating the line strength. The best match is then searched for in the two-dimensional parameter space of the line width and line strength. A good Fe II subtraction is found when the parts of the continuum between the $H\gamma$ and $H\beta$ and between 5100–5400 Å (which covers the Fe II multiplets 48, 49) are flat. The best-fit Fe II template emission lines are then subtracted from the observed spectrum. The Fe II flux is then determined from the best fitting Fe II template between the rest wavelengths 4434 Å and 4685 Å. The procedure of Fe II subtraction is illustrated in Fig. 1. In each panel of Fig. 1, the top curve is the dereddened spectrum, the bottom curve is the Fe II template while the middle curve shows the Fe II-subtracted spectrum. Note that the Fe II-subtracted spectra have been shifted downwards for clarity.

In the BG92 method, it is assumed that the relative strengths of the Fe II lines (within each multiplet and among multiplets) are the same for different objects. For half of our spectra, the Fe II emission can be subtracted very well by the Fe II template. However, for F00275–2859, IRAS 07598+6508, F09427+1929, Mrk 231 and F20036–1547, the Fe II multiplets 48, 49 (5100–5400 Å) are stronger than Fe II multiplets 37, 38 relative to the BG92 template. In contrast, for F02065+4705, F10026+4347, Z11598–0112, F20520–2329 and F22454–1744, the Fe II multiplets 37, 38 (4500–4680 Å) are stronger than Fe II multiplets 48, 49 relative to BG template. For these objects, significant Fe II residuals can be seen in their Fe II-subtracted spectra. The extreme case is Z11598–0112, for which nearly half of the Fe II $\lambda 4570$ (i.e. Fe II multiplets 37, 38) is left after the multiplets 48, 49 are subtracted. Fig. 2 shows two examples of such remarkable Fe II emission residuals in the Fe II multiplets 48, 49 and 37, 38 in the top and bottom panels, respectively. Compared with the optical QSO sample of BG92, the IR QSO sample contains more objects showing large deviations from the Fe II template.

The spectra For F13218+0552 and F23411+0228 are too noisy to detect the Fe II lines reliably, so we take the Fe II strength for F13218+0552 from Remillard et al. (1993) and ignore F23411+0228 in our statistical analysis concerning the Fe II strength.

3.2. Emission Line Fitting and Measurement

As a first step, we use a single Gaussian profile to fit each emission line for all target galaxies. It works well for most emission lines. However, a single Gaussian profile cannot fit some lines, e.g., those with asymmetric profiles. In such cases, two Gaussian components are used to fit the emission lines, namely, one narrow component and one centroid-shifted broad component. The blueshift (or redshift) is defined as the shift of the broad component relative to the narrow component in units of km s^{-1} . Fig. 3 illustrates the two Gaussian component fitting for the permitted line $H\beta$ (top

panel) and forbidden line [O III] $\lambda 5007$ (bottom panel). In Fig. 3, the observed and fitted profiles are shown by the solid and dashed lines, respectively, while the dot-dashed line is for the Gaussian components and the dotted line represents the fitting residual. As one can see, for F01572+0009, the blueshift of the permitted emission line $H\beta$ of F00275–2859 is 750 km s^{-1} while the blueshift of [O III] $\lambda 5007$ is 510 km s^{-1} .

Moreover, there is no correlation between the FWHM of the narrow Gaussian component of the permitted line $H\beta$ and that of the forbidden line [O III] $\lambda 5007$. It implies that the narrow Gaussian component of the permitted emission lines is different from the narrow lines (such as [O III] $\lambda 5007$) from the narrow line region. Efforts were also made to separate the narrow Gaussian component contributed by the narrow line region. However, the contribution from the narrow line region is usually less than 3% so we ignore this component in our discussions.

We also measure the asymmetry parameter defined by de Robertis (1985):

$$\text{asy} = \frac{\lambda_c(3/4) - \lambda_c(1/4)}{\Delta\lambda(1/2)}, \quad (1)$$

where $\lambda_c(1/4)$ and $\lambda_c(3/4)$ are the wavelength centers at 1/4 and 3/4 of the maximum, respectively, and $\Delta\lambda(1/2)$ is the FWHM. The asymmetry parameter is positive (negative) if there is excess light in the blue (red) wing.

Based on the Fe II-subtracted spectra and Gaussian fitting of emission lines, we measured the flux, FWHM, and equivalent width (EW) for each strong emission line for all our objects. The fluxes of broad lines or asymmetric lines refer to the sum of double components. For most targets, the uncertainty of flux measurement of emission lines is about 10%, but for low S/N cases it could be up to 20%. The uncertainty of the blueshift measurement is within 150 km s^{-1} . However, for three sources (F02054+2835, F13218 +0552 and F23411+0228), the fluxes of emission lines have large uncertainties due to the poor S/N and hence they are less reliable.

The dereddened and Fe II-subtracted spectrum for each sample IR QSO is shown in Fig. 1. Table 3 lists the FWHM, blueshifts and asymmetry parameters for $H\beta$ and [O III] $\lambda 5007$. The intrinsic FWHM values are obtained from the subtraction, in quadrature, of the observed FWHM and that of the instrumental profile, measured from the comparison lamp lines. Note that only the significant [O III] $\lambda 5007$ blueshifts (the [O III] $\lambda 5007$ blueshift $> 500 \text{ km s}^{-1}$) are listed. In Table 4, color excess $E(B-V)$, the equivalent widths of the emission lines and various line ratios are listed.

4. Statistical Results

As discussed in the introduction, our sample is a unique one to investigate the physical connection among IR QSO, luminous NLS1s and lo-BAL QSOs. We therefore performed statistical studies similar to those in BG92 for their optical sample, which includes 87 QSOs from the Bright Quasar Survey Catalogue with redshift less than 0.5 (Schmidt & Green 1983). The results for these

two samples will be compared in order to understand any possible evolutionary connection between IR QSOs and classical QSOs.

4.1. The Percentage of NLS1s and Strong Fe II Emitters

It is obvious from Table 3 that for all our IR QSOs except F16136+6550 and F18216+6419, the $H\beta$ FWHM is less than 4000 km s^{-1} . This differentiates IR QSOs from classical QSOs as the main characteristic of classical QSOs is the presence of broad permitted emission lines with typical FWHM between 4000 and 10000 km s^{-1} (Rodríguez-Ardila et al. 2000). To make it clear, Fig. 4 shows the distribution of the $H\beta$ FWHM for our sample (top) and the BG92 sample (bottom). A Kolmogorov-Smirnov (K-S) test indicates a probability of 9.5×10^{-5} for the two distributions being the same. From Table 3 and Fig. 4, the percentage of IR QSOs with $H\beta$ FWHM less than 2000 km s^{-1} in our sample is 60% (15/25). In comparison, only 23% of BG92 QSOs have FWHM $H\beta$ less than 2000 km s^{-1} and one third of BG92 QSOs are classical QSOs with $H\beta$ FWHM larger than 4000 km s^{-1} .

As part of our IR QSOs are selected from the IRAS-ROSAT cross-correlation catalogue, our sample may be biased to include more NLS1s (Stephens 1989). To check this, we performed statistics for the sub-sample of 15 objects selected from two purely IR-selected samples (the QDOT redshift survey and 1 Jy ULIRG sample). Out of these 15 objects, 8 are identified as NLS1s (53%). Therefore, there is no clear difference in the fraction of NLS1s between the whole sample and the purely IR-selected sub-sample.

We also carefully investigated whether the $H\beta$ blueshift could influence the $H\beta$ FWHM and concluded that this possibility is unlikely. Therefore the percentage of NLS1s seems genuinely high in our IR QSO sample.

Fig. 5 shows the histograms of the $\text{Fe II } \lambda 4570/H\beta$ ratio for the IR QSO and BG92 samples. We can see from Fig. 5 that the $\text{Fe II } \lambda 4570/H\beta$ ratio distributions for the two samples are quite different. A K-S test reveals that the probability for these two distributions being the same is 3.0×10^{-6} . Table 4 shows that 25% (6 in 24) and 46% (11 in 24) of IR QSOs are respectively extremely strong ($\text{Fe II } \lambda 4570/H\beta > 2.0$) and moderately strong ($1.0 < \text{Fe II } \lambda 4570/H\beta < 2.0$) Fe II emitters (Joly 1991; Véron-Cetty, Véron-Cetty, & Gonçalves 2001). In contrast, for the BG92 sample, only 15 out of 87 (17%) QSOs are moderately strong Fe II emitters and there are no extremely strong Fe II emitters present. The high percentage of strong Fe II emitters in our sample can also be seen by comparing with that of the overall AGN population. Véron-Cetty et al. (2001) found that moderately strong Fe II emission occurs in only about 5% of AGNs and only a few AGNs are extremely strong Fe II emitters. Furthermore, the two weakest Fe II emitters (with $\text{Fe II } \lambda 4570/H\beta < 0.5$) in our sample (F16136+6550 and F18216+6419) have broad permitted emission lines with FWHM larger than 4000 km s^{-1} , and hence are classical QSOs.

4.2. The Correlations

In this subsection, we study the correlations between various emission lines and continua for our sample IR QSOs. For this purpose, we performed Spearman Rank-order (S-R) correlation analyses among various quantities and investigate the implications of these correlations. As mentioned above, most of our sample IR QSOs are moderately/or extremely strong Fe II emitters, and the origin of the Fe II emission is still not understood. Hence our analysis focuses on the correlations of the Fe II strength with other parameters. Throughout this paper, the correlations are characterized by the probability \mathcal{P} that the null hypothesis of no correlation is true.

Fig. 6 shows the Fe II $\lambda 4570/\text{H}\beta$ line ratio versus the [O III] $\lambda 5007$ peak, defined as the peak height of the [O III] $\lambda 5007$ line relative to that of $\text{H}\beta$ as in PG92. These two parameters are anti-correlated with a correlation coefficient of 0.71 at a very high significance level ($\mathcal{P} = 6.1 \times 10^{-6}$). This result is consistent with BG92 although the correlation between these two parameters is stronger than the one reported by BG92 for optically selected QSOs. The Fe II $\lambda 4570/\text{H}\beta$ ratio is also well correlated with the [O III] $\lambda 5007/\text{H}\beta$ ratio with $\mathcal{P} = 9.8 \times 10^{-3}$. Note that 6 IR QSOs in our sample have very weak [O III] $\lambda 5007$ emission (with EW of [O III] $\lambda 5007$ less than 5 Å). Such a weak [O III] $\lambda 5007$ emission is an important characteristic of lo-BAL QSOs (Boroson & Meyers 1992); we return to this point in §5.2.

Fig. 7 shows the striking correlation between the Fe II $\lambda 4570/\text{H}\beta$ line ratio and the $\text{H}\beta$ blueshift. The S-R correlation coefficient is 0.75 which is highly significant with $\mathcal{P} = 2.7 \times 10^{-5}$. In particular, it can be seen from Table 3 and Fig. 7 that about two thirds of our targets show $\text{H}\beta$ blueshifts with values as large as 2000 km s^{-1} .

As there are striking correlations between both the Fe II $\lambda 4570/\text{H}\beta$ and [O III] $\lambda 5007$ peak and Fe II $\lambda 4570/\text{H}\beta$ and $\text{H}\beta$ blueshift, we also performed a correlation analysis between the [O III] $\lambda 5007$ peak and $\text{H}\beta$ blueshift. We found that these two parameters are well correlated with an S-R correlation coefficient of 0.72 corresponding to $\mathcal{P} = 1.4 \times 10^{-4}$. These tight correlations between the $\text{H}\beta$ blueshift, Fe II $\lambda 4570/\text{H}\beta$ and the [O III] $\lambda 5007$ peak must reflect some physical connection between these lines.

Fig. 8 plots the Fe II $\lambda 4570/\text{H}\beta$ line ratio versus the $\text{H}\beta$ FWHM for 24 of our objects (F23411+0228 is excluded due to its low S/N). If the two classical QSOs with $\text{H}\beta$ FWHM larger than 4000 km s^{-1} are excluded, then the S-R correlation coefficient between these two parameters is 0.47 with $\mathcal{P} = 2.8 \times 10^{-2}$. If we further exclude the 3 objects with $\text{H}\beta$ FWHM larger than 3000 km s^{-1} (but smaller than 4000 km s^{-1}), the correlation becomes somewhat stronger, with an S-R correlation coefficient of 0.58 corresponding to $\mathcal{P} = 9.9 \times 10^{-3}$. We caution, however, that if we include the 2 objects with $\text{H}\beta$ FWHM larger than 4000 km s^{-1} , the Fe II $\lambda 4570/\text{H}\beta$ line ratio and the $\text{H}\beta$ FWHM are no longer well correlated.

Fig. 9 shows the Fe II $\lambda 4570/\text{H}\beta$ line ratio versus the $\text{H}\beta$ asymmetry parameter defined by de Robertis (1985, see also eq. 1). The S-R correlation coefficient is 0.46 with $\mathcal{P} = 2.8 \times 10^{-2}$. Our

result is broadly consistent with BG92, although the $H\beta$ asymmetry parameters for our sample IR QSOs seems to be much larger than those for the BG92 sample. Quantitatively, just 13% of BG92 QSOs have the asymmetry parameter larger than 0.1, while in our sample 48% (26%) of IR QSOs have the $H\beta$ asymmetry value larger than 0.1 (0.2).

As described in §3.2, the $H\beta$ blueshift value is determined by the blueshift of the broad Gaussian component relative to the narrow Gaussian component in permitted emission lines. The blueshifted broad Gaussian component may be connected with the outflow of clouds in the broad line region (Leighly 2001). Outflows with a velocity of several hundred or even a few thousand km s^{-1} could produce shocks that can excite the emission lines. Such shocks may be an important ingredient for understanding the strong correlation seen between the $\text{Fe II } \lambda 4570/H\beta$ ratio and the $H\beta$ blueshift.

4.3. The Soft X-ray Properties

We collected all the X-ray information from Moran et al. (1996) and Xia et al. (2001) based on ROSAT archive data. Table 1 lists the ratio of the soft X-ray luminosity to the infrared luminosity, L_X/L_{FIR} . This is an important quantity as nearly all the luminosity of an ULIRG is emitted in the far-infrared band (Surace et al. 2000). We can see from Table 1 that 17 of our IR QSOs were detected by either ROSAT All Sky Survey (13/17) or pointing observations (4/17). The ratio of the soft X-ray luminosity to the far-infrared luminosity spans about four orders of magnitude. Not surprisingly, the four objects (IRAS 07598+6508, Mrk 231, F00275–2859 and F21219–1757) detected only by ROSAT pointings have the lowest $L_X/L_{\text{FIR}} < 0.01$ values compared with the other 14 objects detected by the ROSAT All Sky Survey. For the non-detections, we calculated their upper limits of the soft X-ray luminosity as follows. We assume a detection limit is 6 source photons (as in the ROSAT All-Sky Survey Faint Source Catalogue, Voges et al. 2000) and an average exposure time of 400 seconds for each source. The spectrum of each source is taken to be a power-law with a photon index of 2.3 (appropriate for AGNs) and Galactic neutral hydrogen column density is adopted. The estimated L_X/L_{FIR} upper limits are also given in Table 1. As might be expected, they all satisfy $L_X/L_{\text{FIR}} < 0.01$.

Fig. 10 shows the $H\beta$ blueshift versus the ratio of soft X-ray luminosity to far-infrared luminosity for 14 objects detected by the ROSAT All Sky Survey and ROSAT pointings. In this statistic and also in the following statistics concerning L_X/L_{FIR} , we excluded F16136+6550, F18216+6419 because they have broad emission lines and are QSOs; F23411+0228 is also excluded due to its low S/N spectrum. It is clear from Fig. 10 that the objects with larger $H\beta$ blueshifts tend to be soft X-ray weak and vice versa (the S-R correlation coefficient -0.61 corresponding to $\mathcal{P} = 2.0 \times 10^{-2}$). In Fig. 10, we also labelled the two potential low-BAL QSOs (F09427+1929 and F20036–1547, see section 5.2) using their soft X-ray luminosity upper limits. These two objects strengthen the trend described above.

During our data reduction, we noticed that the Fe II emission cannot be subtracted very well

by the Fe II template of BG92 for one third of our targets, i.e., there are large residuals of Fe II multiplets 48, 49 (5100–5400 Å) or Fe II multiplets 37, 38 (4500 – 4680 Å) in the Fe II-subtracted spectra. We define the residual of Fe II multiplets 37, 38 (or Fe II 48, 49) as the excess of Fe II 37, 38 (or Fe II 48, 49) relative to its strength in the best-fit Fe II template. A positive residual means that there is an excess in the Fe II 37, 38 while a negative value signals an Fe II 48, 49 excess. The Fe II residual is somewhat uncertain due to the extinction correction. Since the blue light suffers more extinction than the red light, an over-correction in the extinction would lead to an over-estimate of the Fe II multiplets 37, 38 and hence increase the value of the Fe II residual in this multiplets. This overall trend also establishes that the excess of Fe II multiplets 48, 49 relative to multiplets 37, 38 cannot be an artifact. For example, for F00275–2859, we have adopted $E(B-V) = 0.41$, which results in a negative Fe II residual (i.e., there is an excess in the Fe II multiplets 48, 49). If no extinction is adopted, then the value of the Fe II residual in the multiplets 48, 49 would further increase by 30%. We note that while Boroson & Green (1992) have described such residuals, they are not as remarkable as in our IR QSO sample.

We list the measurements of significant Fe II residuals in Table 4. We have examined the correlation of the residuals with other parameters. A correlation was found between the residuals of Fe II multiplets and the soft X-ray luminosity. This is interesting because it ties in with the long-standing puzzle why some NLS1s with extremely strong Fe II emission are X-ray luminous, while others with similar optical spectra are X-ray weak. Fig. 11 shows the residuals of Fe II multiplets vs. the L_X/L_{FIR} ratio for 14 object with concrete X-ray detections. We can see from Fig. 11 that as the residual of Fe II multiplets increases from minus to positive, the soft X-ray luminosities of IR QSOs also increase (the S-R correlation coefficient is 0.44 with the correlation significant of $\mathcal{P} = 0.117$). The most interesting result from Fig. 11 is that objects with larger Fe II multiplets 48, 49 residuals are all X-ray weak. To check the validity of this result, we measured or estimated the Fe II multiplets residual for another two low-redshift lo-BAL QSOs — PG 1700+518 and IRAS 14026+4341. The Fe II multiplets 48, 49 residuals are 0.19 and 0.1, respectively. These two objects are shown in Fig. 11 as well using their upper limits of the soft X-ray luminosity (the soft X-ray information of PG 1700+518 is from Wang, Brinkmann, & Bergeronet 1996). In the same figure, we also indicated the locations of two potential lo-BAL QSOs, F09427+1929 and IRAS 20036–1547, as they have significant Fe II multiplets 48, 49 residuals and extremely weak [O III] $\lambda 5007$. It is interesting that all four low-redshift lo-BAL QSO and the two potential low-BAL IR QSOs are located in the bottom left of Fig. 11. Furthermore, we also measured the Fe II multiplets residual for soft X-ray weak QSOs (Brandt, Laor & Wills 2000) with available spectral data. None of them have positive Fe II multiplets residuals. It appears that the Fe II multiplets residual may be a good criterion to select X-ray weak QSOs or lo-BAL QSOs.

4.4. Infrared Properties

The infrared color-color diagram has been used as an important tool to discriminate starbursts and AGN activities in the nuclear/circumnuclear regions of galaxies (de Grijp et al. 1985; L  pari 1994). 20 IR QSOs in our sample are securely detected in three far-infrared bands (25, 60 and $100\mu\text{m}$). Fig. 12 shows the location of these objects in the infrared color-color diagram, $\alpha(60, 25)$ versus $\alpha(100, 60)$. Here $\alpha(\lambda_1, \lambda_2) = -\log(F(\lambda_2)/F(\lambda_1))/\log(\lambda_2/\lambda_1)$, where the wavelength is in units of μm . In the same diagram, the power-law and blackbody lines are also indicated.

It is clear from Fig. 12 that almost all IR QSOs except F13218+0552 are located between the blackbody and power-law lines. Moreover, there are a group of IR QSOs clearly located close to the blackbody line. This group includes F01572+0009, IR06269–0543, F11119+3257, F13218+0552, F15462–0450, F23411+0228 and Mrk 231. We find that they have either significant [O III] $\lambda 5007$ blueshifts (see Table 3), or significant [O II] $\lambda 3727$ blueshifts (Mrk 231, see L  pari et al. 2002).

The objects close to the power-law line are F18216+6419, F16136+6550, F12265+0219 (3C 273), F10026+4347, F22454–1744 and three additional objects in the bottom left of the figure. The first 2 objects are the only classical QSOs in our sample while the remaining objects are all moderate/extremely strong Fe II emitters with bright soft X-ray emission (see Table 4).

5. Summary and Discussion

We studied an IR QSO sample with a total of 25 objects. The sample is compiled from the QDOT redshift survey, the 1 Jy ULIRGs survey and from a cross-correlation study of the IRAS Point Source Catalogue with the ROSAT All Sky Survey Catalogue. Using the observed optical spectra and archive data in the infrared and soft X-ray, we investigated the correlations of the Fe II $\lambda 4570/\text{H}\beta$ ratio with the [O III] $\lambda 5007$ peak, $\text{H}\beta$ blueshift and the $\text{H}\beta$ FWHM. All these parameters are correlated. We found that soft X-ray weak QSOs, especially lo-BAL QSOs, tend to have significant Fe II multiplets 48, 49 (5100–5400 Å) residuals (cf. Fig. 11). The correlation between the Fe II $\lambda 4570/\text{H}\beta$ residuals and the L_X/L_{FIR} ratio, shown in Fig. 11, although somewhat weak, may be a useful clue for understanding why some strong/extremely strong Fe II emitters are X-ray luminous while others are X-ray quiet.

5.1. The Outflows

One of the striking features of the emission lines for IR QSOs is the blueshift of permitted emission lines or the forbidden [O III] $\lambda 5007$ line. As we have removed the Fe II multiplets carefully surrounding the $\text{H}\beta$ and [O III] $\lambda\lambda 4959, 5007$, there should not be much Fe II multiplet contamination to the $\text{H}\beta$ and [O III] $\lambda\lambda 4959, 5007$ emission lines. Moreover, the blueshifts measured from $\text{H}\beta$ and $\text{H}\alpha$ are similar, as are the blueshifts measured from the [O III] $\lambda 5007$ and [O III] $\lambda 4959$ lines (see

Fig. 3). The asymmetries of the $H\beta$ and $[O\ III]\ \lambda 5007$ lines cannot be attributed to contaminations from other emission lines. Outflows give a plausible explanation for the emission line blueshift (for alternative explanations, see Brandt et al. 2000). Such emission-line outflows have been found and discussed extensively for some NLS1s (Leighly 2000; Christopoulou et al. 1997), radio galaxies (Tadhunter et al. 2001) and for IR QSOs (Lípari 2002).

From the strong correlation between the Fe II FWHM and the $H\beta$ FWHM, Boroson & Green (1992) suggested that the Fe II line and permitted emission lines share a common emission region. If the $H\beta$ blueshifts are due to cloud outflows in the broad line region, shocks are likely to be produced in outflows. Such shocks may be responsible for the Fe II emission, as the pure photoionization model fails to explain the strong Fe II emission (Collin & Joly 2000). The tight correlation between the $H\beta$ blueshift and the Fe II $\lambda 4570/H\beta$ ratio can then be understood as they are physically connected through shocks associated with outflows. Analogously, the $[O\ III]\ \lambda 5007$ blueshifts could probe the outflows in narrow line emission region. It is interesting to see that all objects with large $[O\ III]\ \lambda 5007$ blueshifts are located close to the blackbody line in the infrared color-color diagram. Hence the locations of IR QSOs in the infrared color-color diagram may be related with outflows in the $[O\ III]\ \lambda 5007$ emission line region. We caution, however, that there are other explanations concerning the strong Fe II emission, especially in NLS1 galaxies (see Sulentic, Marziani, & Dultzin-Hacyan 2000 for a review).

If the emission line blueshifts can indeed be attributed to outflows, then our sample indicates such outflows are common for IR QSOs. Our statistics do not however clarify which mechanism (central AGN radiative pressure, starbursts or both) drives these outflows. High resolution observations and investigations in the UV, soft X-ray and optical bands are needed to further explore this unique sample.

5.2. The Connection of IR QSOs with Luminous NLS1s and Low-ionization BAL QSOs

60% of our IR QSOs satisfy the strict criteria of NLS1s. For the remaining objects, most are moderate strong/extremely strong Fe II emitters. However, 71% (5/7) of the extremely strong Fe II emitters in IR QSO sample fail to meet the strict criterion of NLS1s. Similarly, a large fraction (44%) of extremely strong Fe II emitters in the sample of Véron-Cetty et al. (2001) also have $H\beta$ FWHM larger than $2000\ \text{km s}^{-1}$. As Véron-Cetty et al. (2001) pointed out, there should be a continuous distribution of optical line widths for QSOs/Seyfert 1s and hence the separation between the broad line Seyfert 1s and NLS1s at $2000\ \text{km s}^{-1}$ could be arbitrary (see also Sulentic et al. 2000). Our results seem to support the above statement and hint that the strength of optical Fe II emission line, rather than the $H\beta$ FWHM, may be the most important characteristic of non-classical QSOs.

Much attention has been paid to lo-BAL QSOs recently. Canalizo & Stockton (2001b) stud-

ied four lo-BAL QSOs currently known at $z < 0.4$ and found that all four are ULIRGs which reside in dusty starbursts or post-starbursts. Two of these, Mrk 231 (i.e., F12540+5708) and IRAS 07598+6508, are in our IR QSO sample. The main characteristics of lo-BAL QSOs are strong Fe II emissions, very weak [O III] $\lambda 5007$ emissions and low X-ray luminosity. They are immediately located between the power-law and blackbody lines in the infrared color-color diagram (cf. Fig. 12). A recent Chandra survey for BAL QSOs also revealed that all these four lo-BAL QSOs have high column densities and are unusually faint in both soft and hard X-ray bands (Gallagher et al. 2002). These properties are shared by some other IR QSOs in our sample in addition to Mrk 231 and IRAS 07598+6508. For example, F00275–2859, F09427+1929 and F20036–1517 have all the properties of lo-BAL QSOs as described above. We identify them as potential or more evolved lo-BAL QSOs. If UV observations establish that they are real lo-BAL QSOs, the percentage of lo-BAL QSOs in our sample will be 20%, similar to the fraction found by Boroson & Meyers (1992) for a much smaller IR QSO sample.

Brandt & Gallagher (2000) argued that the potential physical connection between luminous NLS1s and lo-BAL QSOs is their high accretion rate relative to the Eddington accretion rate. IR QSOs tend to appear in the final merging phase with their central AGN activity recently triggered or rejuvenated by the merging activity (Sanders & Mirabel 1996; Zheng et al. 1999; Canalizo & Stockton 2001a and reference therein). Numerical simulations show that a large amount of gas flows toward the center during mergers (e.g., Barnes & Hernquist 1991), so it seems plausible that IR QSOs also have high accretion rates. Such systems may have a greater ability to drive radiative outflows. The correlations we presented in section 4.2 suggest that the outflow velocity and the physical condition in the outflow region (inferred from the $H\beta$ and [O III] $\lambda 5007$ emission line blueshifts) influence the Fe II, infrared and soft X-ray emission properties. In short, IR QSOs, luminous NLS1s and lo-BAL QSOs may have some common physical conditions. The difference between them may be from different viewing angles or from different evolution phases. A careful study of IR QSOs may be important for understanding the evolution and formation of classical QSOs.

We are grateful to Drs. Th. Boller, T.Q. Wang, J.Y. Wei, L.C. Deng and Mr. Z.H. Shang for helpful discussions, and to the BATC members for advice on data deduction. Particular thanks are due to Drs T. Boroson & R. Green for kindly providing their Fe II template and their dataset of QSOs in PG92. We also thank the anonymous referee and Dr. Richard James for constructive comments that improved the paper. This project was supported by NSF of China and NKBRSF G19990754.

REFERENCES

- Baker, J. C. MNRAS, 286, 23
- Barnes, J. E., & Hernquist, L. E. 1991, ApJ, 370, L65
- Boller, Th., Brandt, W. N., & Fink, H. 1996, A&A, 305, 53
- Boller, Th., Meurs, E. J. A., Brinkmann, W., Fink, H., Zimmermann, U., & Adorf, H.-M. 1992, A&A, 261, 57
- Borne, K. D., et al. 1999, Ap&SS, 266, 137
- Boroson, T. A., & Green, R. F. 1992, ApJS, 80, 109 (BG92)
- Boroson, T. A., & Meyers, K. A. 1992, ApJ, 397, 442
- Brandt, W. N., & Gallagher, S. C. 2000, NewAR, 44, 461
- Brandt, W. N., Laor, A., & Wills, B. J. 2000, ApJ, 528, 637
- Canalizo, G., & Stockton, A. 2001a, ApJ, 555, 719
- Canalizo, G., & Stockton, A. 2001b, preprint (astro-ph/0107323)
- Christopoulou, P. E., Holloway, A. J., Steffen, W., Mundell, C. G., Thean, A. H. C., Goudis, C. D., Meaburn, J., & Pedlar, A. 1997, MNRAS, 284, 385
- Clements, D. L., Sutherland, W. J., Saunders, W., Efstathiou, G. P., McMahon, R. G., Maddox, S., Lawrence, A., & Rowan-Robinson, M. 1996, MNRAS, 279, 459
- Collin, S., & Joly, M. 2000, NewAR, 44, 531
- Cui, J., Xia, X. Y., Deng, Z. G., Mao, S., & Zou, Z. L. 2001, AJ, 122, 63
- de Grijp M. H. K., Miley, G. K., Lub, J., & de Jong, T. 1985, Nature, 314, 240
- de Robertis, M. 1985, ApJ, 289, 67
- Farrah, D., et al. 2001, MNRAS, 326, 1333
- Gallagher, S. C., Brandt, W. N., Chartas, G., & Garmire, G. P. 2002, ApJ, in press (astro-ph/0110579)
- Genzel, R., et al. 1998, ApJ, 498, 579
- Grupe, D., Beuermann, K., Mannheim, K., & Thomas, H.-C. 1999, A&A, 350, 805
- Grupe, D., Beuermann, K., Thomas, H.-C., Mannheim, K., & Fink, H. H. 1998, A&A, 330, 25

- Joly, M. 1991, *A&A*, 242, 49
- Kim, D.-C., & Sanders, D. B., 1998, *ApJS*, 119, 41
- Kim, D.-C., Veilleux, S., & Sanders, D. B., 1998, *ApJ*, 508, 627
- Lawrence, A., Walker, D., Rowan-Robinson, M., Leech, K. J., & Penston, M. V. 1986, *MNRAS*, 219, 687
- Lawrence, A., Elvis, M., Wilkers, B. J., McHardy, I., & Brandt, N. 1997, *MNRAS*, 285, 879
- Lawrence, A., et al. 1999, *MNRAS*, 308, 897
- Leighly, K. M. 2001, in *ASP Conf. Ser. 224, Probing the Physics of Active Galactic Nuclei*, ed. B. M., Peterson, R. W., Pogge, & R. S., Polidan (San Francisco: ASP), 293
- Lípari, S. 1994, *ApJ*, 436, 102
- Lípari, S., et al. 2002, preprint (astro-ph/0007316)
- MacAlpine, G. M., 1985, *Astrophysics of Active Galaxies and Quasi-stellar Objects* (Mill Valley: USB)
- Moran, E. C., Halpern, J. P., & Helfand, D. J. 1996, *ApJS*, 106, 341
- Moshir, M., et al. 1992, *Explanatory Supplement to the IRAS Faint Source Survey, Version 2*, JPL D-10015 8/92 (Pasadena: JPL)
- Osterbrock, D. E. 1989, *Astrophysics of Gaseous Nebulae and Active Galactic Nuclei* (Mill Valley: USB)
- Osterbrock, D.E., & Pogge, R.W. 1985, *ApJ*, 297, 166
- Remillard, R.A., Bradt, H.V.D., Brissenden, R.J.V., Buckley, D.A.H., Roberts, W., Schwartz, D.A., Stroozas, B.A., & Tuohy, I.R. 1993, *AJ*, 105, 2079
- Rodríguez-Ardila, A., Pastoriza, M.G., & Donzelli, C.J. 2000, *ApJS*, 126, 63
- Sanders, D. B. 2001, *IAU Colloq.*, 184, ed. R. F., Green, E. Ye., Khachikian, & D. B., Sanders (Byurakan: ASP), 29
- Sanders, D. B. & Mirabel, I. F. 1996, *ARA&A*, 34, 749
- Sanders, D. B., Soifer, B. T., Elias, J. H., Madore, B. F., Matthews, K., Neugebauer, G. & Scoville, N. Z. 1988, *ApJ*, 325, 74
- Saunders, W., et al. 2000, *MNRAS*, 317, 55
- Schmidt, M., & Green, R. F. 1983, *ApJ*, 269, 352

- Stephens, S. A. 1989, *AJ*, 97, 10
- Sulentic, J. W., Marziani, P., & Dultzin-Hacyan, D. 2000, *ARA&A*, 38, 521
- Sulentic, J. W., Zwitter, T., Marziani, P., & Dultzin-Hacyan, D. 2000, *ApJ*, 536, L5
- Surace, J. A., Sanders, D. B., Vacca, W. D., Veilleux, S., & Mazzarella, J. M. 1998, *ApJ*, 492, 116
- Surace, J. A., Sanders, D. B., & Evans, A. S. 2000, *ApJ*, 529, 170
- Tadhunter, C., Wills, K., Morganti, R., Oosterloo, T., & Dickson, R. 2001, *MNRAS*, 327, 227
- Veilleux, S., Kim, D.-C., & Sanders, D. B. 1999, *ApJ*, 522, 113
- Veilleux, S. & Osterbrock, D. E. 1987, *ApJS*, 63, 295
- Véron-Cetty, M.-P., Véron, P., & Gonçalves, A. C. 2001, *A&A*, 372, 730
- Voges, W. et al. 2000, *Rosat All-Sky Survey Faint Source Catalogue*, *IAU Circ.*, 7432, 3
- Wang, T., Brinkmann, W., & Bergeron, J. 1996, *A&A*, 309, 81
- Weymann, R. J., Morris, S. L., Foltz, C. B., & Hewett, P. C. 1991, *ApJ*, 373, 23
- Wu, H., Zou, Z. L., Xia, X. Y., & Deng, Z. G. 1998, *A&AS*, 132, 181
- Xia, X. Y., Boller, Th., Deng, Z. G., & Börner, G. 2001, *ChJAA*, 1, 221
- Zheng, Z., Wu, H., Mao, S., Xia, X. Y., Deng, Z. G., & Zou, Z. L. 1999, *A&A*, 349, 735

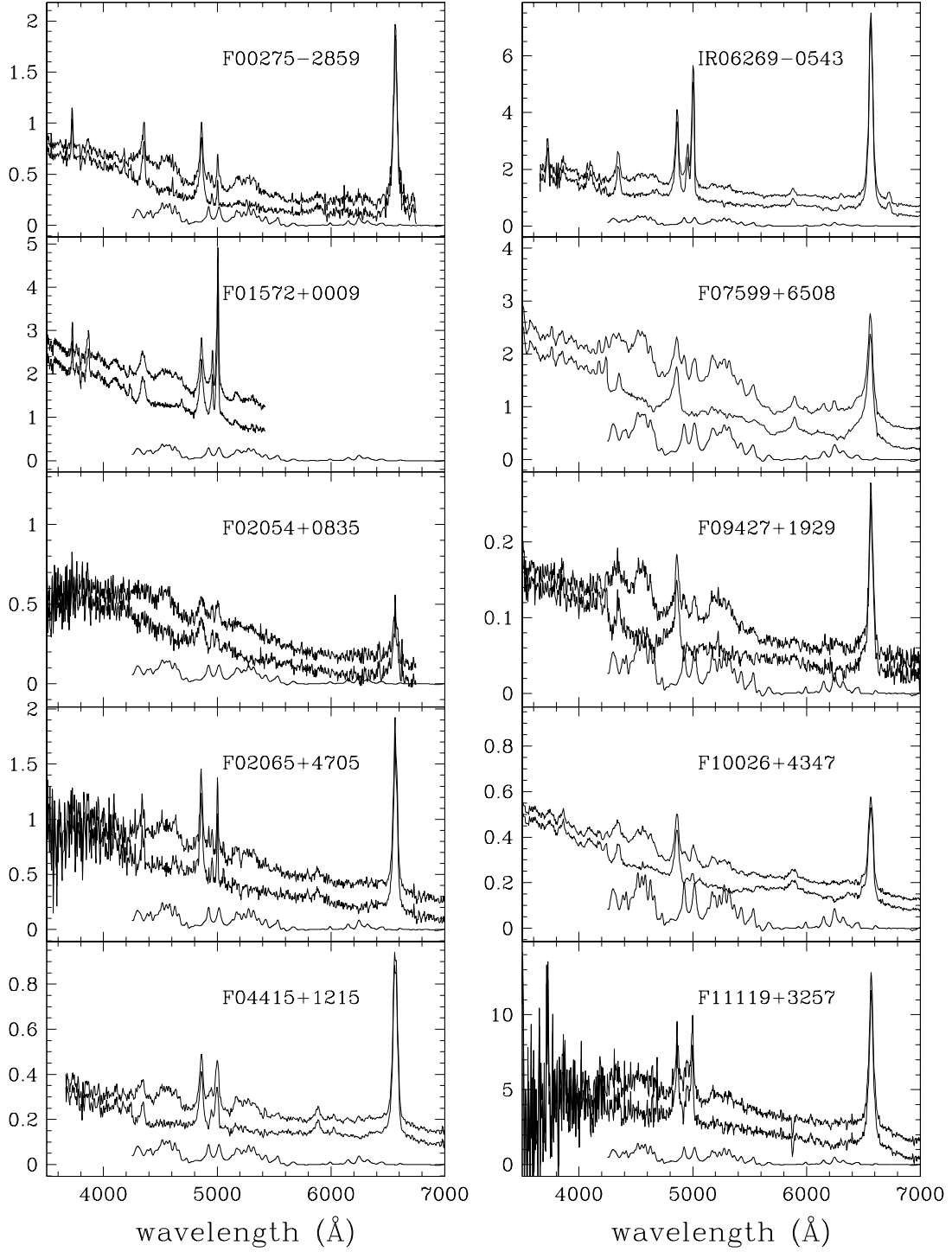


Fig. 1.— Dereddened spectra (top curves), Fe II-subtracted spectra (middle curves) and Fe II spectra (bottom curves) of 25 IR QSOs, shown in increasing order of right ascension. The Fe II-subtracted spectra have been shifted downwards for clarity. The vertical axis shows the observed flux in units of $10^{-15} \text{ erg cm}^{-2} \text{ s}^{-1} \text{ Å}^{-1}$. The horizontal axis is wavelength in Å in the rest frame.

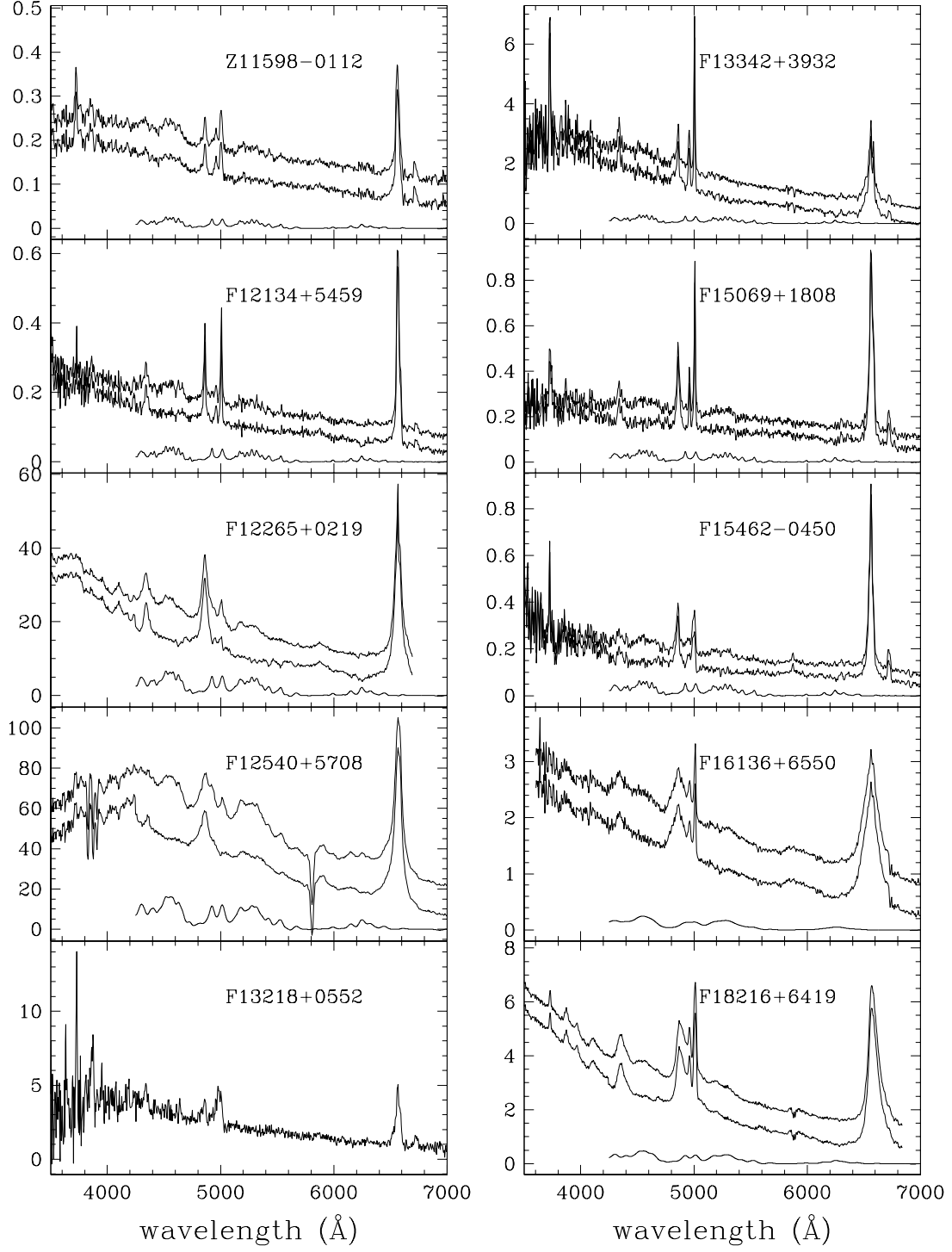


Fig. 1.— Continued.

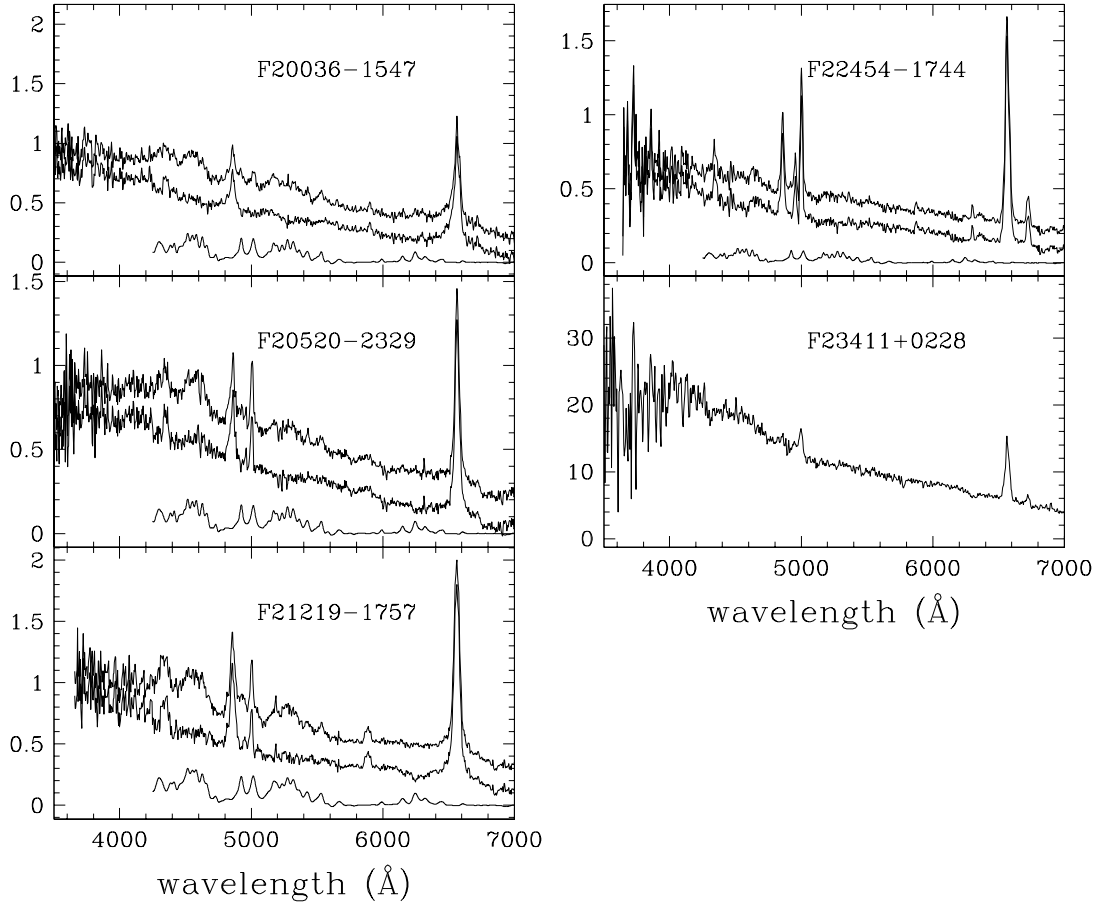


Fig. 1.— Continued.

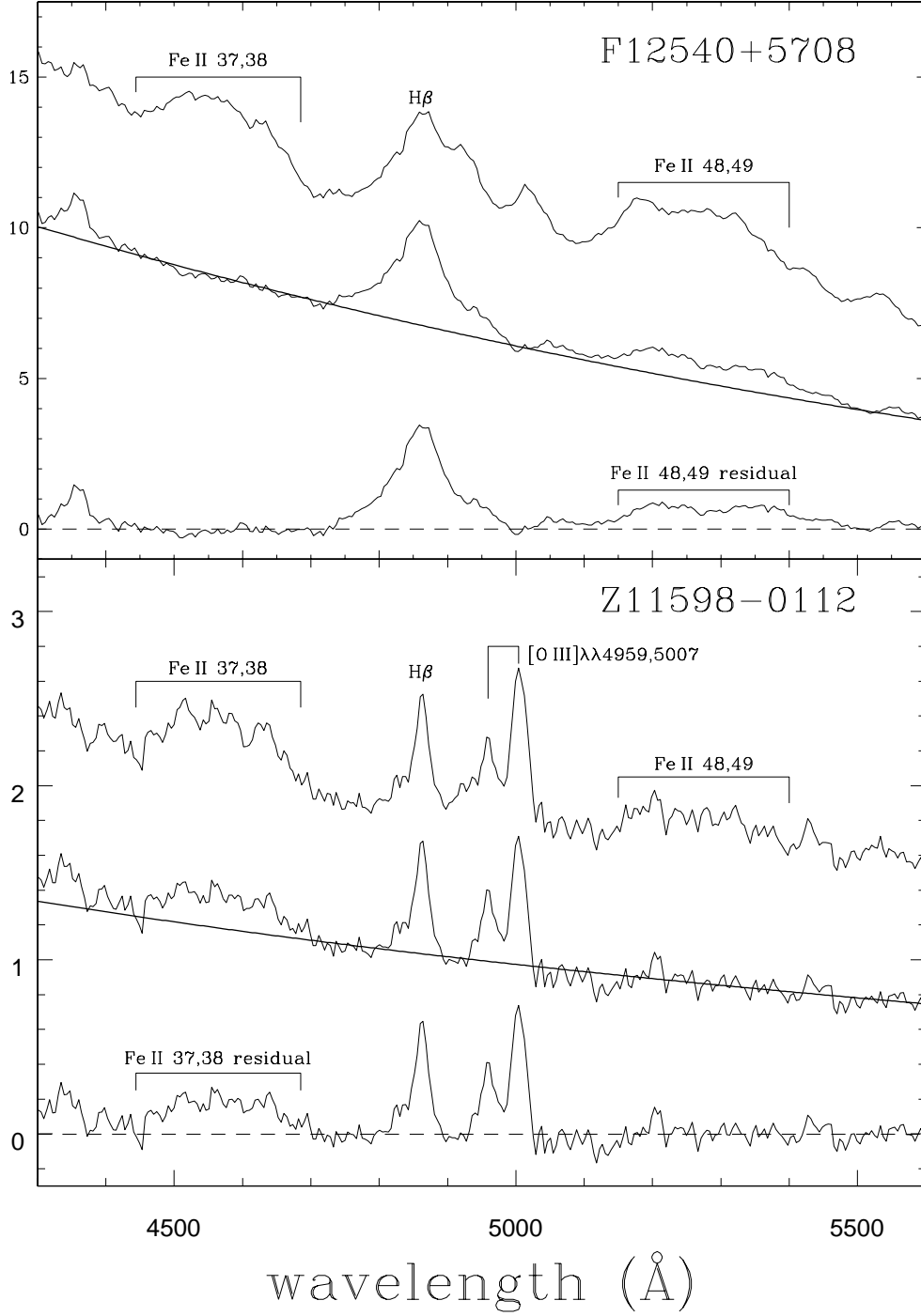


Fig. 2.— Illustration of significant Fe II multiplets residuals. Top panel: F12540+5708 shows the Fe II multiplets 48, 49 residual compared with the Fe II Boroson & Green (1992) template. Bottom panel: Z11598–0112 shows Fe II multiplets 37, 38 residual. In each panel, the top curve is the dereddened observed spectrum between 4300–5100 Å. The middle one show the Fe II-subtracted spectrum (with an arbitrary offset) with the fitted low-order polynomial continuum shown as a thick solid line. The excess of Fe II emission lines is illustrated in the continuum-subtracted bottom curve.

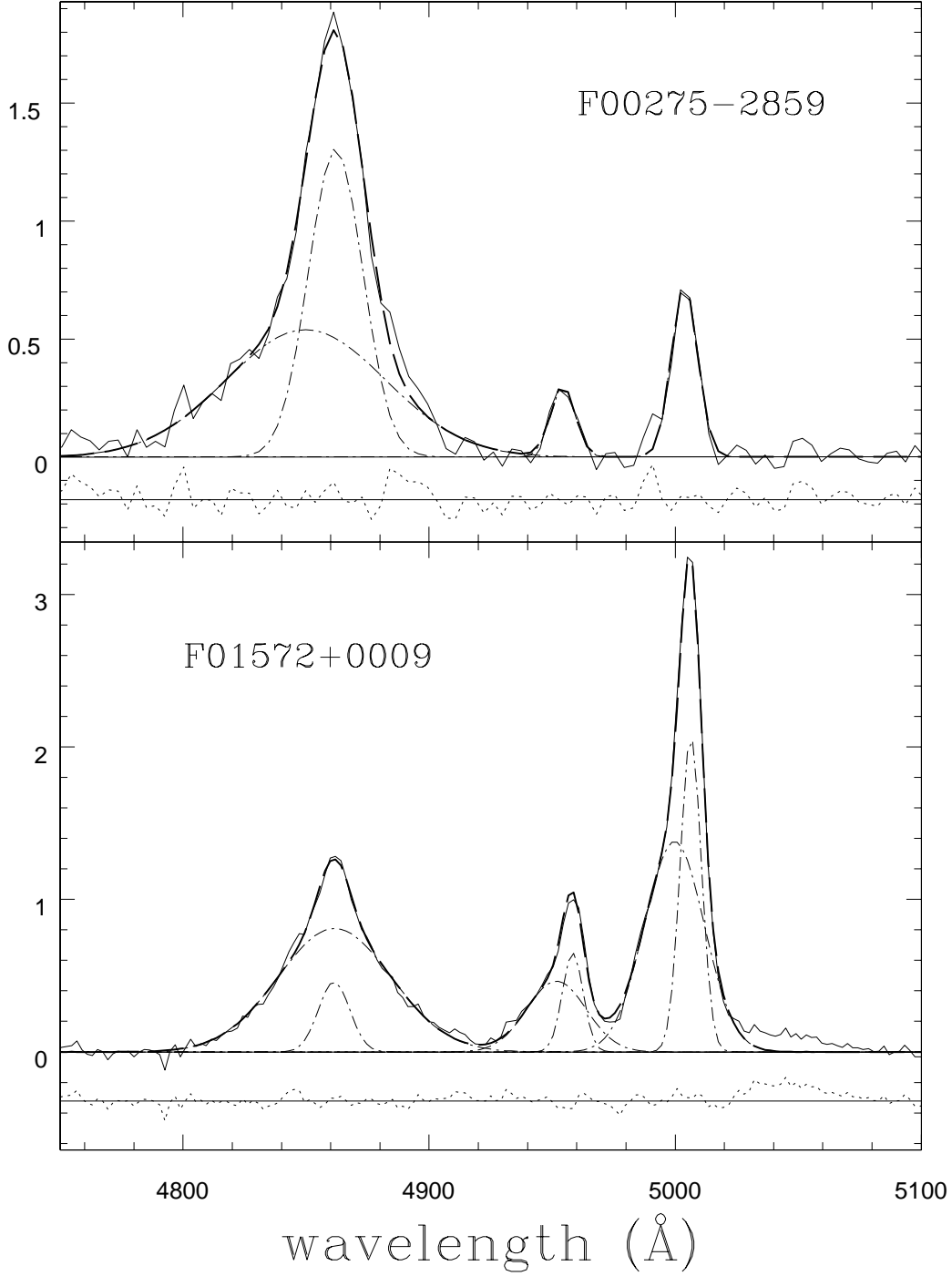


Fig. 3.— Illustration of the blueshifted H β and [O III] $\lambda\lambda 4959, 5007$ lines. Top panel: For F00275-2859, H β can be well fitted by a sum of two Gaussian components with the broad component blueshifted by 750 km s $^{-1}$ relative to the narrow one. Bottom panel: For F01572+0009, [O III] $\lambda\lambda 4959, 5007$ shows a narrow component in addition to a blueshifted broad component. The solid line is the observed profile. The dashed line shows the fitted profile. Each fitted component is shown by a dot-dashed line and the dotted line illustrates the residual of fitting.

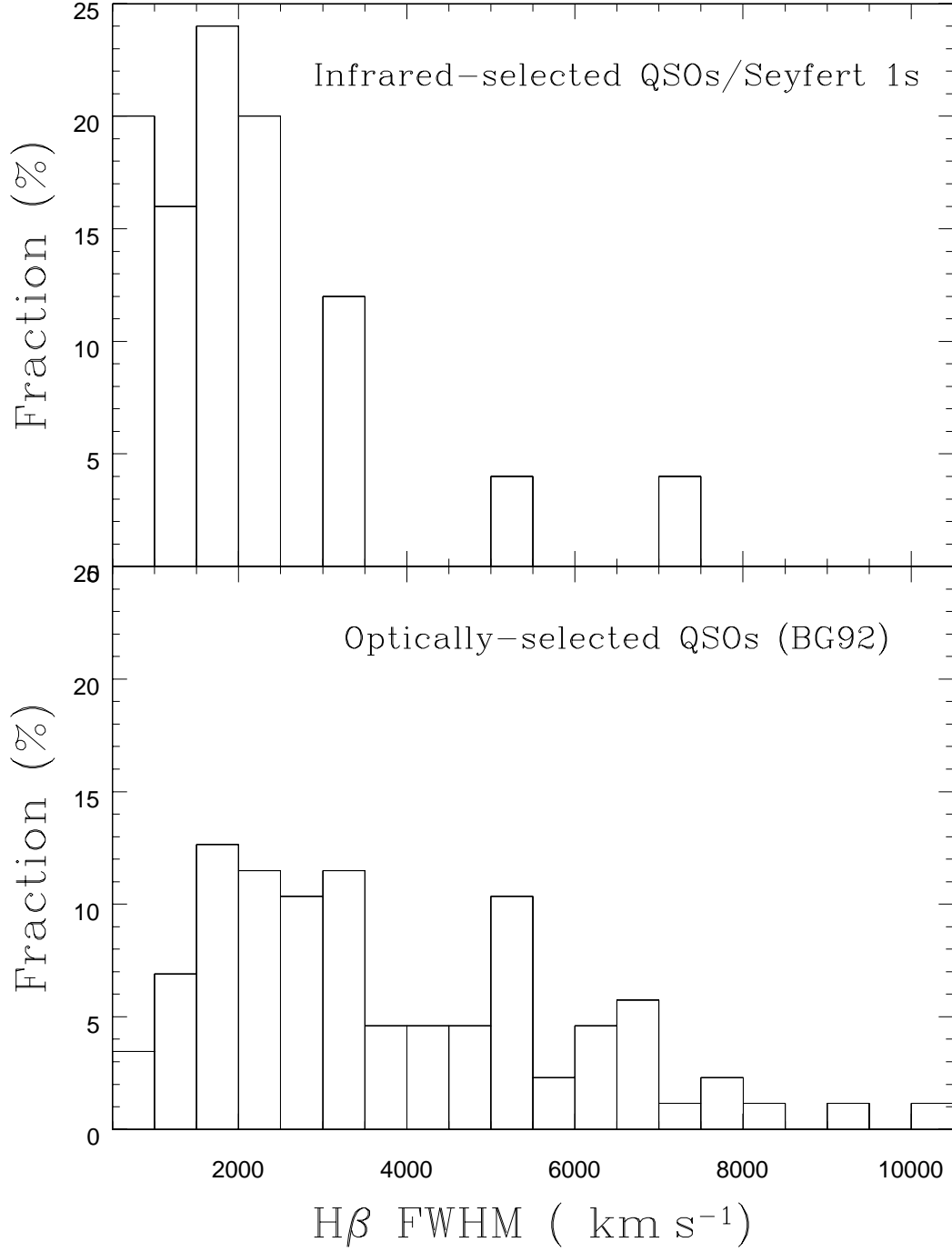


Fig. 4.— Histograms of the $H\beta$ FWHM for IR QSOs (top panel) and for the Boroson & Green sample (bottom panel), which includes 87 optically selected bright QSOs.

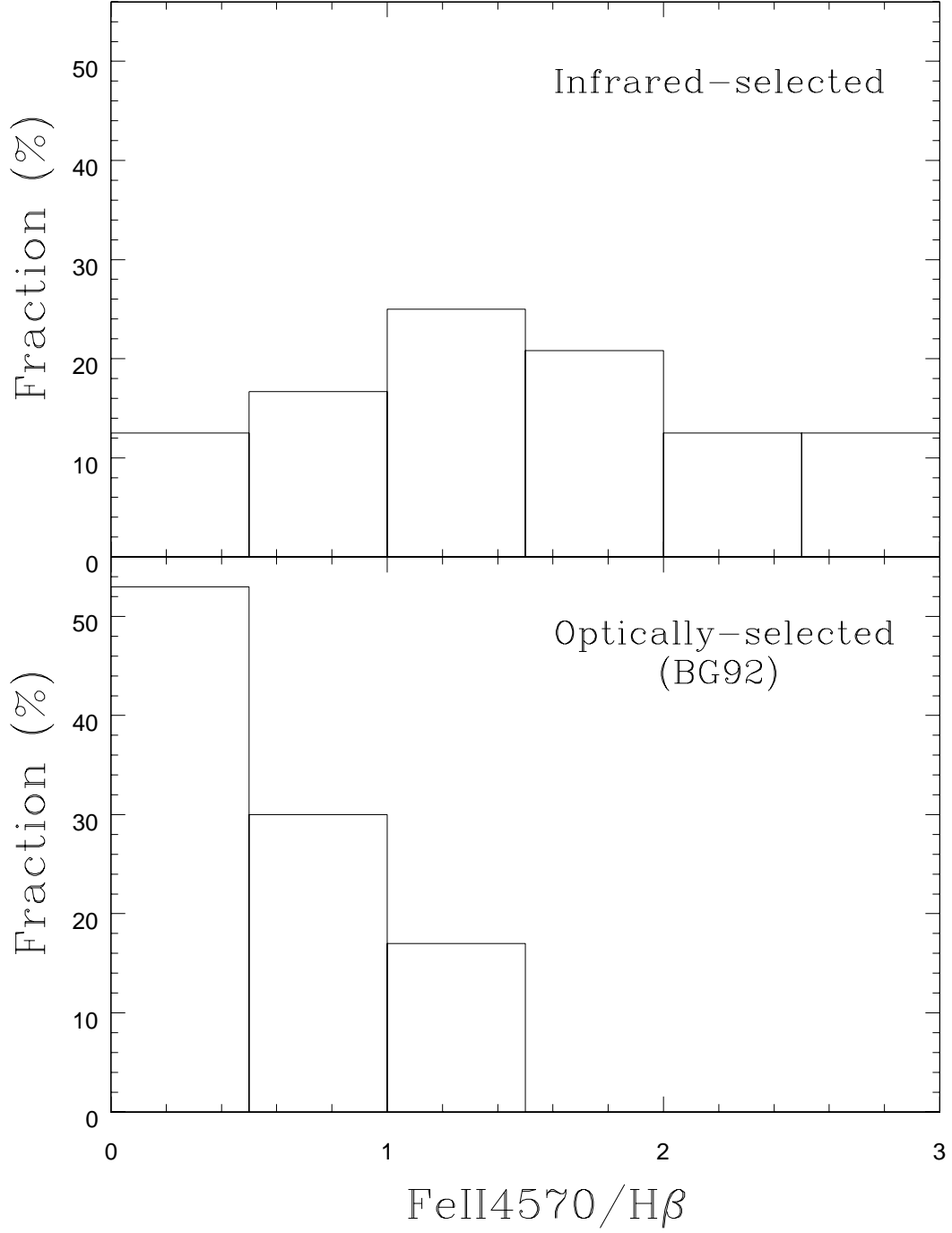


Fig. 5.— Histograms of the $\text{Fe II } \lambda 4570/\text{H}\beta$ ratio for IR QSOs (top panel) and the BG92 sample (bottom panel).

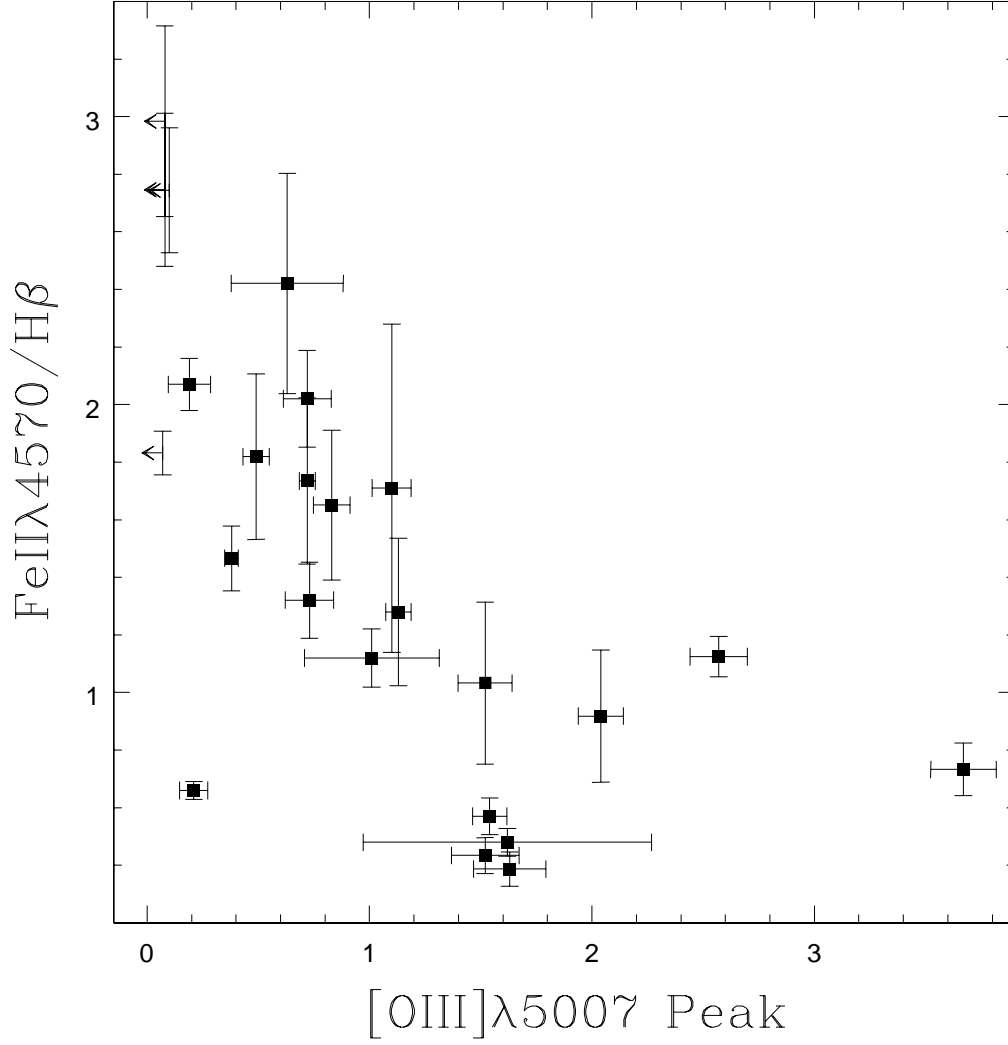


Fig. 6.— Fe II $\lambda 4570$ /H β vs. the ratio of the peak height of [O III] $\lambda 5007$ to that of H β . Upper limits for the non-detections are indicated by arrows. For the detected objects, the Spearman Rank-order correlation coefficient is -0.78 with $\mathcal{P} = 6.1 \times 10^{-6}$, i.e., the probability for the null hypothesis of no correlation between these two parameters being true is 6.1×10^{-6} .

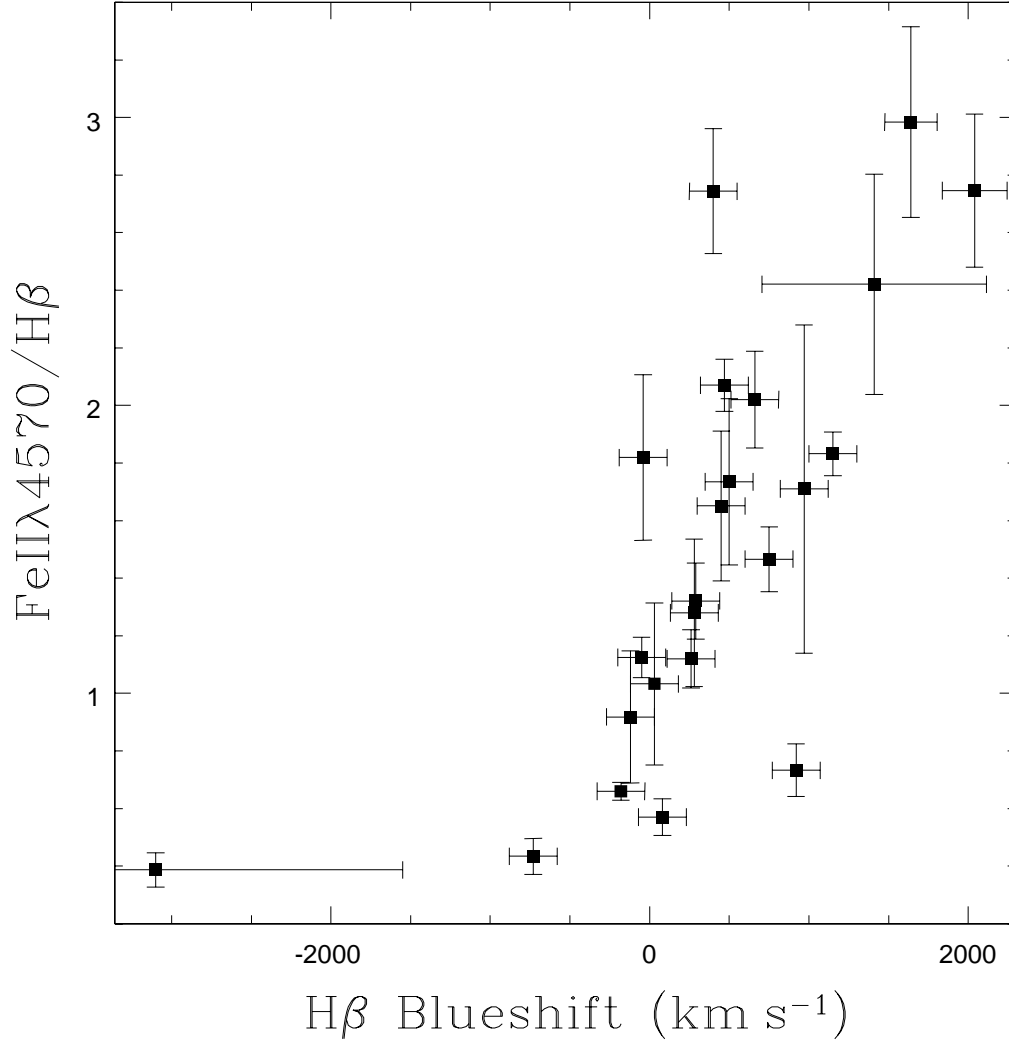


Fig. 7.— Fe II $\lambda 4570$ /H β vs. the H β blueshift, which is defined as the blueshift of the H β broad component relative to the H β narrow component in unit of km s $^{-1}$. A negative value indicates a redshift. For 23 objects, the correlation coefficient is 0.76 with $\mathcal{P} = 2.7 \times 10^{-5}$.

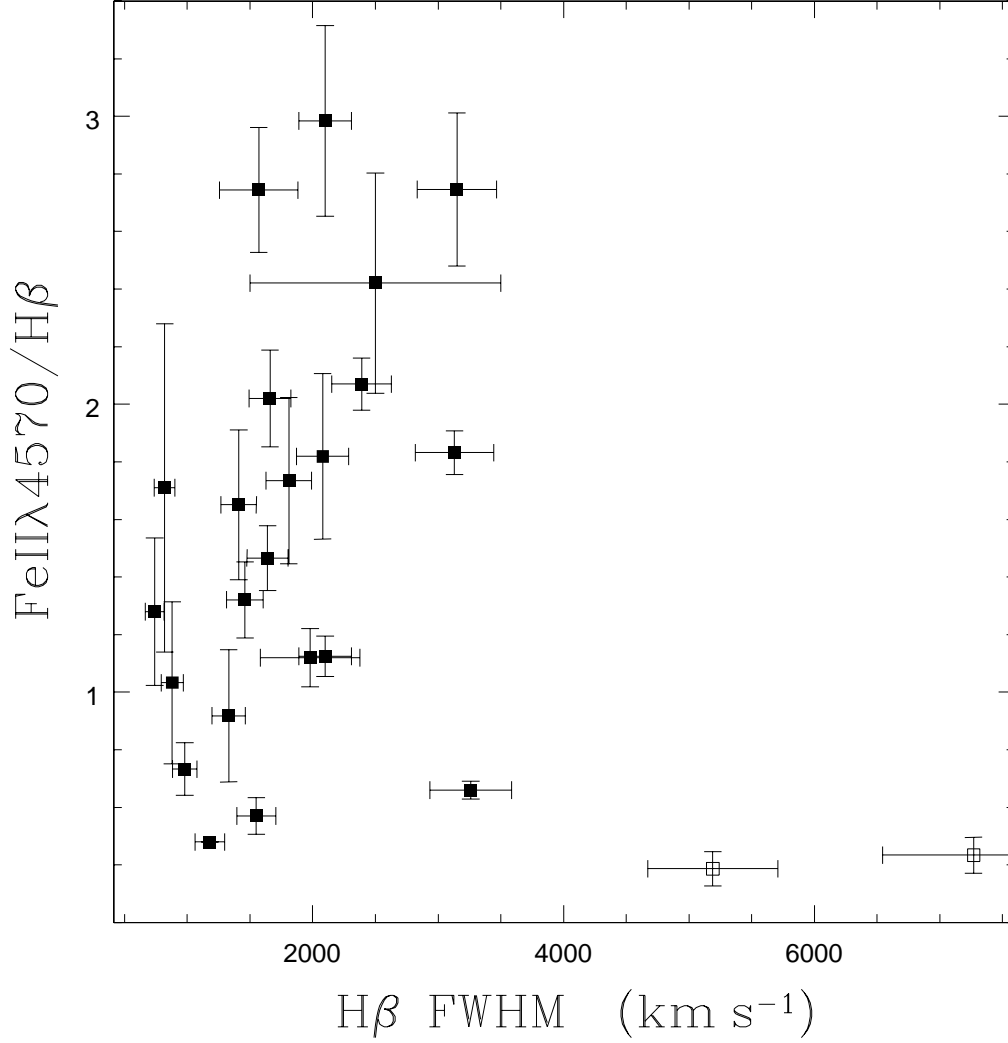


Fig. 8.— Fe II $\lambda 4570$ /H β vs. H β FWHM. The 22 Objects with H β FWHM less than 4000 km s^{-1} are shown as filled squares while the two objects with H β FWHM greater than 4000 km s^{-1} are shown with open squares. The Spearman Rank-order correlation coefficient for the objects with FWHM smaller than 3000 km s^{-1} (4000 km s^{-1}) is 0.47 (0.58) corresponding to $\mathcal{P} = 2.8 \times 10^{-2}$ ($\mathcal{P} = 9.9 \times 10^{-3}$). No correlation is apparent if we include all objects. Note that F23411+0228 is excluded due to its low S/N spectrum.

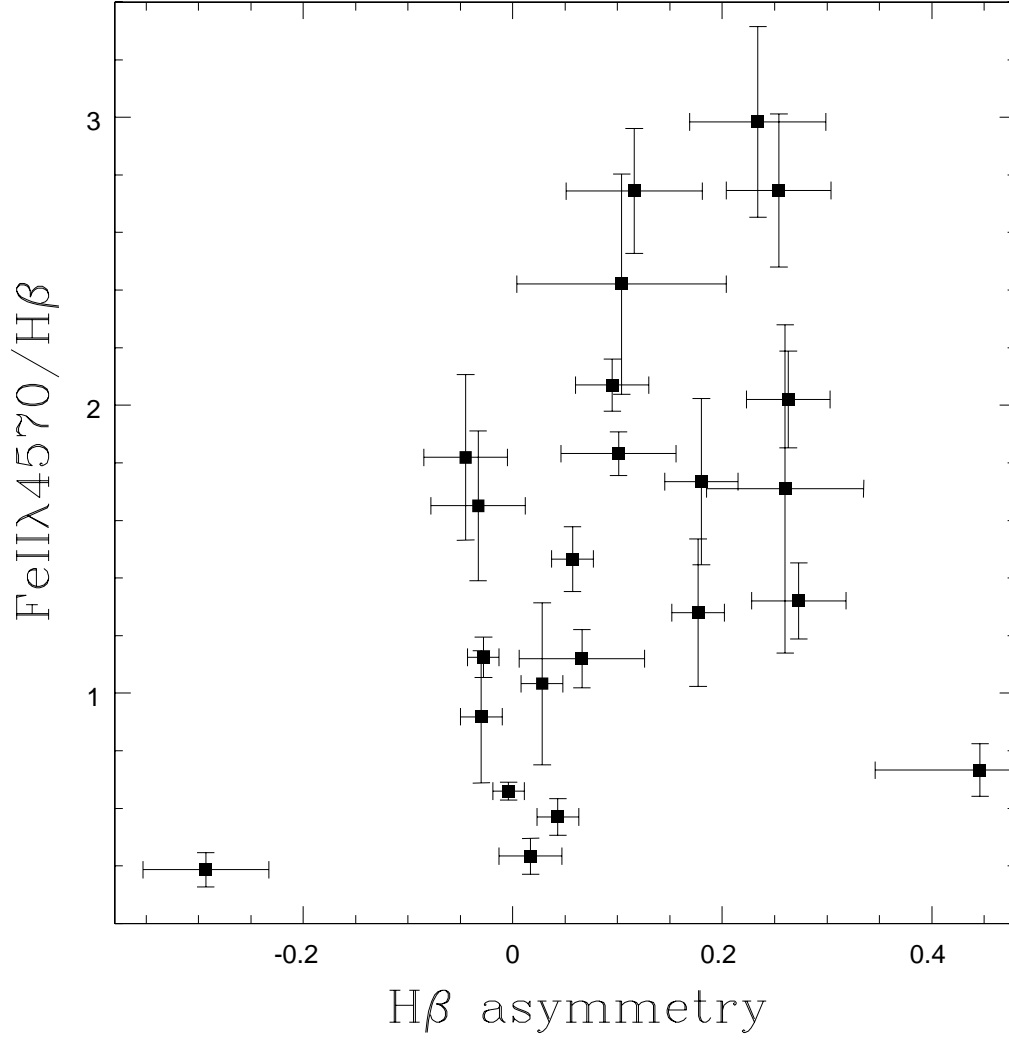


Fig. 9.— Fe II $\lambda 4570$ /H β vs. the H β asymmetry index defined by de Robertis (1985, cf. eq. 1). The correlation coefficient is 0.46 corresponding to $\mathcal{P} = 2.8 \times 10^{-2}$.

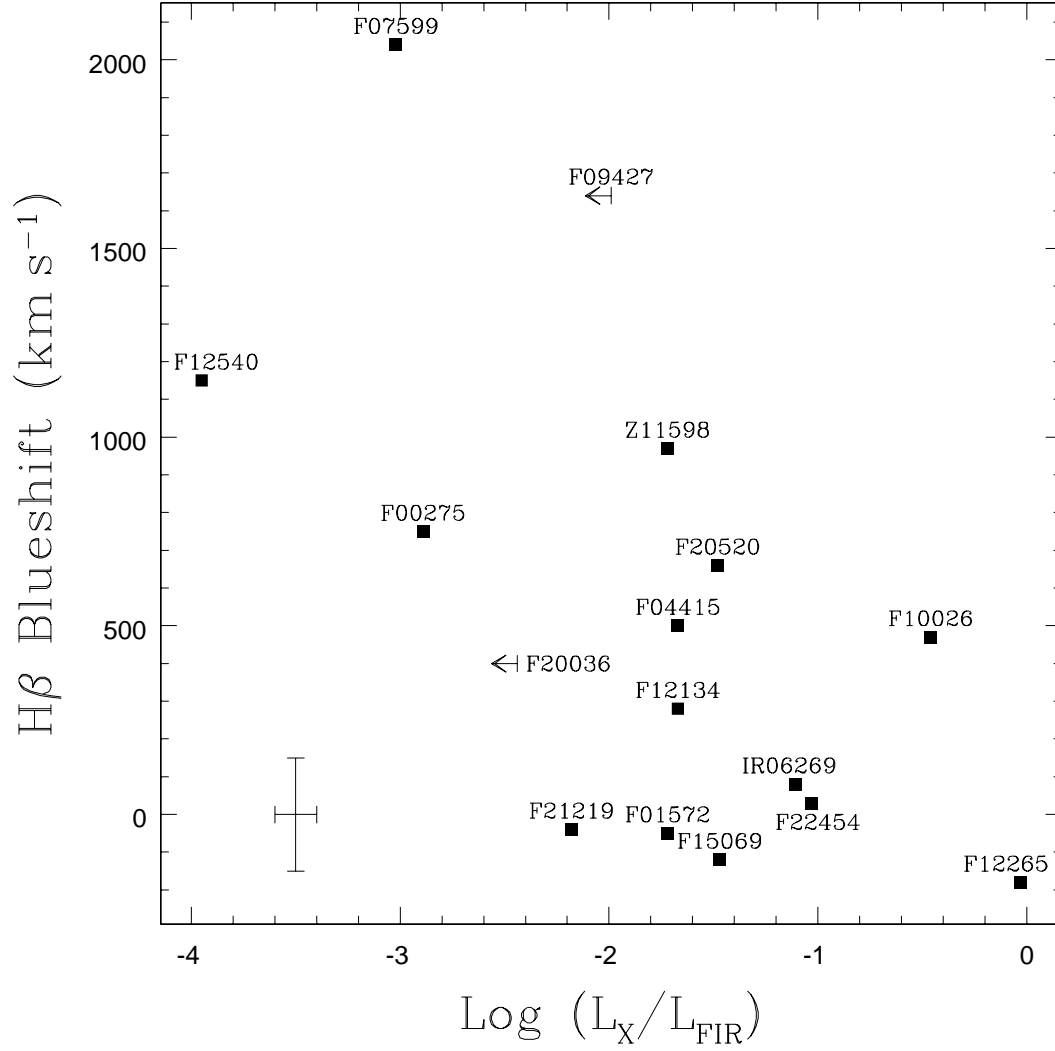


Fig. 10.— H β blueshift vs. soft X-ray luminosity for 14 objects (filled squares) detected by the ROSAT All Sky Survey or Pointings. The correlation coefficient for the detected objects is -0.61 with $\mathcal{P} = 2.0 \times 10^{-2}$. Additionally, two potential lo-BAL QSOs are marked by arrows with their upper limits of X-ray luminosity (see text). Typical error bars are indicated in the lower-left.

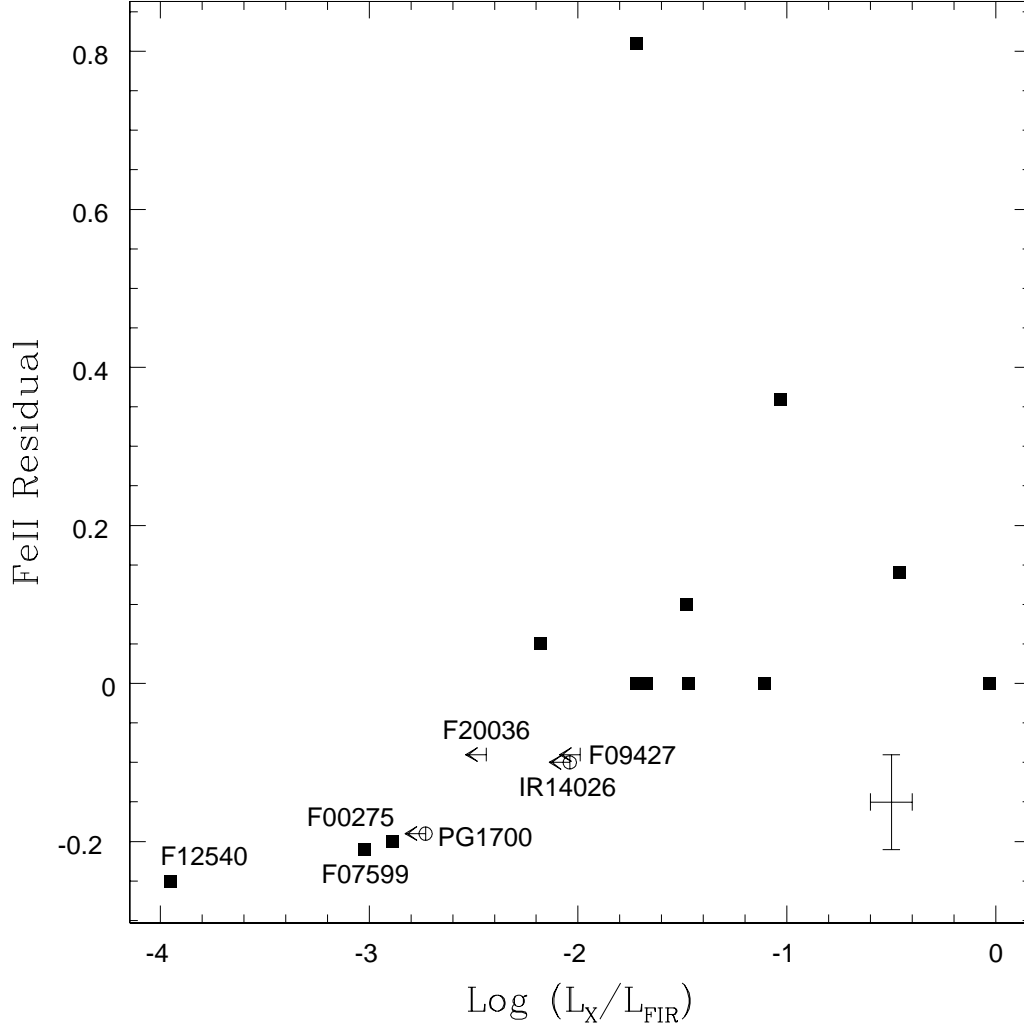


Fig. 11.— Fe II residual vs. L_X/L_{FIR} . The Fe II residual is defined in the text (see section 4.3). The arrows with a circle indicate upper limits for additional lo-BAL QSOs while those without a circle are for potential lo-BAL QSOs. For the 14 ROSAT detected objects (filled squares), the correlation coefficient is 0.44 with $\mathcal{P} = 0.117$. Typical error bars are indicated in the lower-right.

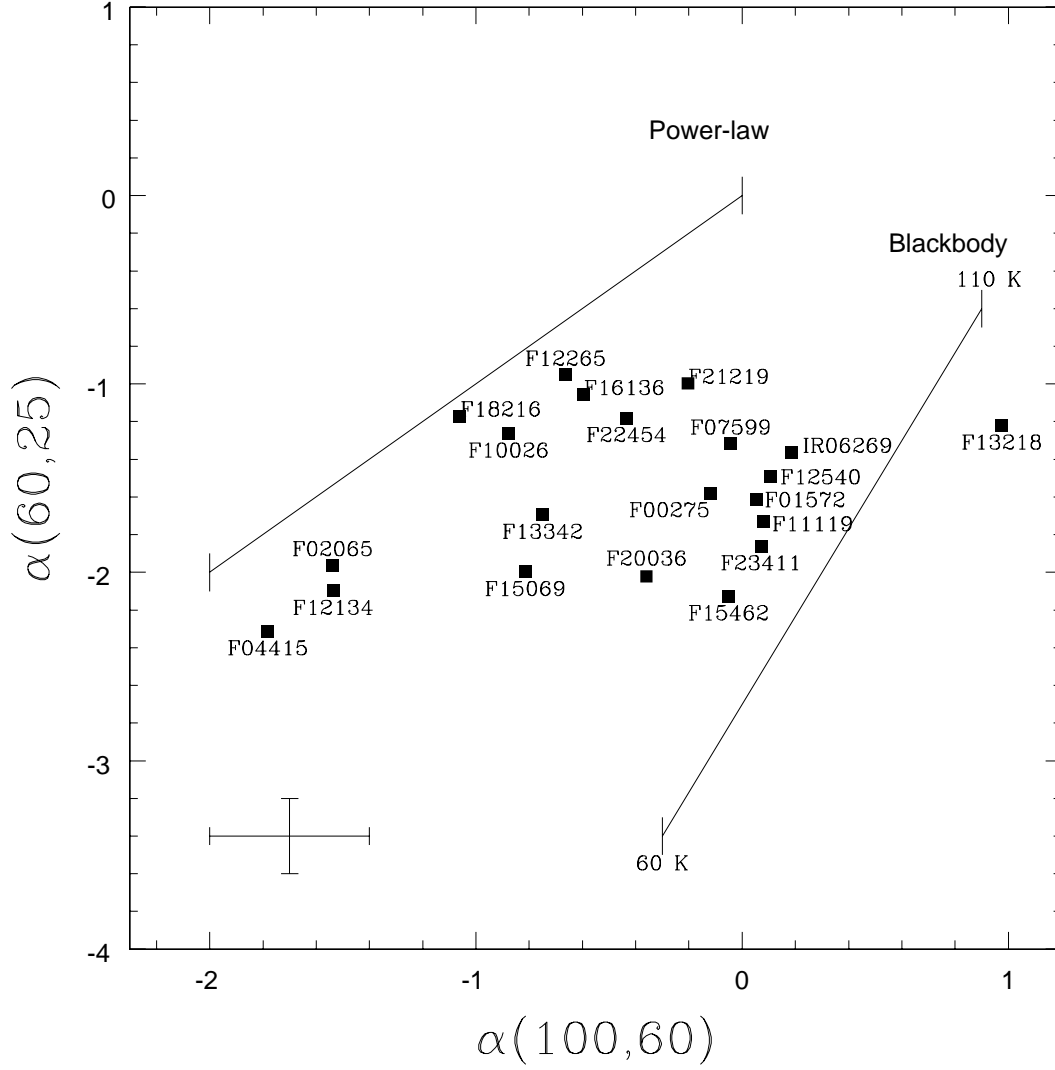


Fig. 12.— IRAS color-color diagram. Our sample galaxies fall in the region between the power-law and blackbody lines. The objects close to the blackbody line all have significant [O III] $\lambda 5007$ blueshifts.

Table 1: Sample of IR QSOs Selected from ULIRGs.

IRAS Name	R.A.	Decl.	$\text{Log}\left(\frac{L_{\text{FIR}}}{L_{\odot}}\right)$	$\text{Log}\left(\frac{L_{\text{IR}}}{L_{\odot}}\right)$	$\text{Log}\left(\frac{L_{\text{X}}}{L_{\text{IR}}}\right)$	Redshift	Ref.
(1)	(2)	(3)	(4)	(5)	(6)	(7)	(8)
F00275–2859	00 30 04.2	–28 42 24.6	12.64	12.90	–2.89	0.279	(1)
F01572+0009	01 59 50.2	+00 23 42.2	12.65	12.85	–1.72	0.163	(2)
F02054+0835	02 08 06.8	+08 50 05.2	12.97	13.29	< –2.17	0.345	(1)
F02065+4705	02 09 45.8	+47 19 43.2	12.27	12.45	< –2.47	0.132	(1)
F04415+1215	04 44 28.8	+12 21 13.1	12.41	12.53	–1.67	0.089	(3)
IR06269–0543	06 29 24.7	–05 45 26.0	12.49	12.74	–1.11	0.117	(3)
F07599+6508	08 04 30.4	+64 59 53.3	12.45	12.77	–3.02	0.148	(2)
F09427+1929	09 45 27.6	+19 15 42.1	12.61	12.90	< –1.99	0.284	(4)
F10026+4347	10 05 41.8	+43 32 41.6	12.20	12.54	–0.46	0.178	(1)
F11119+3257	11 14 38.8	+32 41 34.7	12.64	12.88	< –2.40	0.189	(2)
Z11598–0112	12 02 26.6	–01 29 15.3	11.91	12.43	–1.72	0.151	(2,3)
F12134+5459	12 15 49.3	+54 42 24.6	12.17	12.36	–1.67	0.150	(3)
F12265+0219	12 29 06.6	+02 03 09.0	12.65	13.04	–0.03	0.158	(2,3)
F12540+5708	12 56 13.9	+56 52 24.6	12.60	12.82	–3.95	0.042	(1,2)
F13218+0552	13 24 19.9	+05 37 04.6	12.53	12.94	< –2.23	0.205	(2)
F13342+3932	13 36 24.0	+39 17 32.2	12.49	12.72	< –2.30	0.179	(2)
F15069+1808	15 09 13.7	+17 57 11.0	12.24	12.47	–1.47	0.171	(3)
F15462–0450	15 48 56.8	–04 59 33.5	12.35	12.50	< –2.68	0.101	(2)
F16136+6550	16 13 57.1	+65 43 11.0	11.92	12.24	–0.21	0.129	(3)
F18216+6419	18 21 57.1	+64 20 37.4	13.02	13.34	–0.73	0.297	(3)
F20036–1547	20 06 31.9	–15 39 05.8	12.70	12.89	< –2.44	0.193	(1)
F20520–2329	20 54 57.3	–23 18 24.8	12.52	12.77	–1.48	0.206	(3)
F21219–1757	21 24 41.6	–17 44 45.3	12.02	12.39	–2.18	0.113	(2)
F22454–1744	22 48 04.1	–17 28 28.5	11.94	12.37	–1.03	0.117	(3)
F23411+0228	23 43 39.7	+02 45 05.7	12.14	12.34	–1.98	0.091	(3)

Note. — The Prefix of the object name indicates the origin of IRAS fluxes. ‘F’ refers to the IRAS Faint Source Catalogue and ‘Z’ means the Faint Source Reject File (see Moshir et al. 1992). For IR06269–0543, the IRAS fluxes come from the IRAS Point Source Catalogue. Units of right ascension are hours, minutes, and seconds, and units of declination are degrees, arcminutes, and arcseconds (J2000.0). Col.(4) & (5): far-infrared & infrared luminosity, calculated following Sanders & Mirabel (1996); Col.(6): Soft X-ray luminosity (0.2–2.4 keV) normalized to far-infrared luminosity; Col.(7): redshift, taken from the references.

References. — (1) Lawrence et al. 1999; (2) Kim & Sanders 1998; (3) Moran et al. 1996; (4) Zheng et al. 1999.

Table 2: Journal of Observations.

IRAS Name	Date	Exp.Time (second)	Slit (arcsec)	Seeing (arcsec)
F00275–2859	1999 Nov 07	3600	3.0	3.0
F01572+0009	1996 Nov 17	3600	3.0	3.0
F02054+0835	1998 Oct 22	2700	3.0	2.1
F02065+4705	1999 Feb 20	1800	2.2	1.5
F04415+1215	1998 Oct 18	3600	3.0	3.5
IR06269–0543	1998 Oct 23	1800	3.0	2.1
F07599+6508	1997 Mar 16	3600	3.0	1.5
F09427+1929	1998 Dec 20	3600	2.5	1.5
F10026+4347	1999 Feb 22	3600	2.2	1.5
F11119+3257	1999 Feb 21	2400	2.2	1.5
Z11598–0112	1997 Mar 12	5400	3.0	3.0
F12134+5459	1999 Feb 22	2700	2.2	1.5
F12265+0219	1995 Mar 13	600	3.0	3.0
F12540+5708	1997 Mar 16	1200	3.0	1.5
F13218+0552	1999 Feb 21	3600	2.2	2.0
F13342+3932	1999 Feb 22	1500	2.2	1.5
F15069+1808	1999 Feb 22	1200	2.2	1.5
F15462–0450	1997 Apr 11	3600	3.0	2.0
F16136+6550	1998 Oct 20	1800	3.0	2.1
F18216+6419	1998 Oct 17	2700	2.5	3.5
F20036–1547	1997 Oct 03	2400	2.5	3.5
F20520–2329	1998 Oct 22	2700	3.0	2.1
F21219–1757	1998 Oct 20	2700	3.0	2.1
F22454–1744	1998 Oct 20	2700	3.0	2.1
F23411+0228	1997 Oct 04	4800	2.5	3.5

Table 3: Profile properties of $H\beta$ and $[O\ III]\ \lambda 5007$.

IRAS Name	$H\beta$			$[O\ III]\ \lambda 5007$	
	FWHM (km s^{-1})	Blueshift (km s^{-1})	asy	FWHM (km s^{-1})	Blueshift ^a (km s^{-1})
(1)	(2)	(3)	(4)	(5)	(6)
F00275–2859	1640	750	0.057	710	
F01572+0009	2100	–50	–0.028	680	510
F02054+0835	2500;	1410;	0.104	1300;	
F02065+4705	1410	450:	–0.033	500	
F04415+1215	1810	510	0.180	1240	
IR06269–0543	1550	80	0.043	1210	550
F07599+6508	3150	2030	0.254	...	
F09427+1929	2100	1640	0.234	...	
F10026+4347	2390	470	0.095	810	
F11119+3257	1980:	260:	0.066	1480:	950;
Z11598–0112	820	970	0.260	550	
F12134+5459	740	280	0.177	780	
F12265+0219 ^b	3260	–180:	–0.004	1330:	1020
F12540+5708	3130	1150	0.101	...	
F13218+0552	1180 ^c	1530;	500;
F13342+3932	980	920	0.446	540	
F15069+1808	1330	–120	–0.030	630	
F15462–0450	1460	290:	0.273	1720:	1110:
F16136+6550 ^b	7270	–730:	0.017	920	780
F18216+6419 ^b	5190	–3100;	–0.293	1360	
F20036–1547	1570:	400:	0.116	...	
F20520–2329	1660	660	0.263	300	560:
F21219–1757	2080	–40	–0.045	1360	460:
F22454–1744	880	30	0.028	790	
F23411+0228	970 ^c	1390;	500;

^aFor sources that have an obvious asymmetric $[O\ III]\ \lambda\lambda 4959, 5007$ profile.

^bCases with broad $H\beta$ line; they could be fitted satisfactorily with three Gaussian components.

^cFWHM of $H\alpha$.

Note. — The uncertainty on the FWHM is typically of order 10% ($\sim 200\ \text{km s}^{-1}$). Colons (:) indicate values with a relative uncertainty of 20%. Semicolons (;) indicate values with a relative uncertainty 30%–40%. The typical uncertainty of the blueshift is $\lesssim 150\ \text{km s}^{-1}$. Colons (:) indicate values with a relative uncertainty of 30%. Semicolons (;) indicate values with a relative uncertainty of larger than 50%.

Table 4: Emission Lines Properties.

IRAS Name	E(B–V)	$\frac{\text{Fe II}}{\text{H}\beta}$	Fe II residual	$\lambda 5007$ Peak	$\frac{[\text{O III}]}{\text{H}\beta}$	$\frac{[\text{O II}]}{\text{H}\beta}$	$\frac{[\text{N II}]}{\text{H}\alpha}$	H α EW	H β EW	Fe II EW	[O III] EW	[O II] EW
(1)	(2)	(3)	(4)	(5)	(6)	(7)	(8)	(9) (\AA)	(10) (\AA)	(11) (\AA)	(12) (\AA)	(13) (\AA)
F00275–2859	0.41	1.47	–0.20	0.38	0.14	0.23	<0.01	453.0	75.6	110.8	10.7	7.5
F01572+0009	0.00	1.13	0.0	2.57	1.05	0.11	<0.01		43.5	49.0	45.8	2.8
F02054+0835	0.58:	2.42:	–0.06	0.63:	0.28:	<0.16	0.04:	169.3:	33.4:	80.9:	9.2:	<3.1
F02065+4705	0.25	1.65	0.12	0.83	0.35	<0.06	0.01	189.7	38.4	63.5	13.6	<1.4
F04415+1215	0.11	1.74	0.0	0.72	0.55	<0.05	0.12	209.7	50.9	88.3	28.0	<1.6
IR06269–0542	0.39	0.57	0.0	1.54	1.02	0.21	<0.01	404.0	83.6	47.6	85.2	12.2
F07599+6508	0.00	2.75	–0.21	<0.08	<0.02	<0.04	<0.01	258.3	47.2	129.6	<1.1	<1.3
F09427+1929	0.00	2.98	–0.09	<0.08	<0.02	<0.02	0.08	222.0	52.0	155.1	< 1.1	<0.6
F10026+4347	0.00	2.07	0.14	0.19	0.10	<0.01	<0.01	149.4	36.2	75.0	3.8	<0.1
F11119+3257	1.08	1.12	0.0	1.01	0.75	0.64	0.12	181.8	51.1	57.2	38.5	25.9
Z11598–0112	0.01	1.71	0.81	1.10	0.75	0.88	0.26	69.8	13.9	24.0	10.5	8.6
F12134+5459	0.14	1.28	0.0	1.13	0.68	0.12	0.17	148.4	33.4	42.7	22.8	7.6
F12265+0219	0.00	0.66	0.0	0.21	0.06	<0.02	0.07	299.8	78.3	51.4	4.9	<0.8
F12540+5708	0.65	1.83	–0.25	<0.07	<0.01	<0.13	0.04	257.2	35.0	60.0	<4.1	<3.2
F13218+0552	0.54	0.48 ^a	...	1.62:	2.40 ^a	...	0.28:	162.7	47.7:	...
F13342+3932	0.76	0.73	0.0	3.67	1.09	0.83	0.11	203.2	35.0	25.6	38.0	17.5
F15069+1808	0.01	0.92	0.0	2.04	1.03	0.44	0.18	189.0	46.0	42.2	47.2	13.7
F15462–0450	0.28	1.32	0.0	0.73	0.66	0.48	0.30	126.7	48.7	64.3	32.2	13.5
F16136+6550	0.17	0.43	0.0	1.52	0.20	<0.03	<0.01	325.3	60.0	26.0	11.7	<1.1
F18216+6419	0.00	0.39	0.0	1.63	0.29	0.04	0.04	435.6	79.9	30.9	22.9	1.7
F20036–1547	0.20	2.74	–0.09	<0.10	<0.01	<0.15	0.19	122.9	24.2	66.4	<0.3	<2.4
F20520–2329	0.46	2.02	0.10	0.72	0.37	0.12	0.33	103.2	28.0	56.5	10.3	2.3
F21219–1757	0.23	1.82	0.05	0.49	0.25	<0.07	0.32	153.8	44.2	80.5	11.2	<1.7
F22454–1744	0.21	1.03	0.36	1.52	1.08	0.71	0.17	166.4	33.2	34.3	35.8	15.3
F23411+0228	0.71:	0.08	59.0

^afrom Remillard et al. 1993.

Note. — The typical uncertainty of the emission line fluxes is about 10–20%. The values flagged with colon have uncertainties larger than 40%. Upper limits are given if the emission lines are not convincingly detected. No measurement is listed for the emission lines contaminated by noise. Col.(1): source name, same as in table 1; Col.(2): color excess; Col.(3): strength of Fe II $\lambda 4570$ relative to H β ; Col.(4): relative strength of Fe II residual, positive indicates excess of Fe II $\lambda 37,38$ and negative indicates excess of Fe II $\lambda 48,49$ (cf Fig.2); Col.(5): peak height of [O III] $\lambda 5007$ relative to that of H β ; Col.(6): strength of [O III] $\lambda 5007$ relative to H β ; Col.(7): strength of [O II] $\lambda 3727$ relative to H β ; Col.(8): strength of [N II] $\lambda 6583$ relative to H α ; Col.(9): equivalent width of H α ; Col.(10): equivalent width of H β ; Col.(11): equivalent width of Fe II $\lambda 4570$; Col.(12): equivalent width of [O III] $\lambda 5007$; Col.(13): equivalent width of [O II] $\lambda 3727$.